Effects of Surface Coupling Strength in WRF/Noah-MP Model on Regional Climate Simulations Over China

Xia Zhang (zhangxia@tea.ac.cn)
Institute of Atmospheric Physics Chinese Academy of Sciences https://orcid.org/0000-0002-3784-0498

Liang Chen
Institute of Atmospheric Physics Chinese Academy of Sciences

Zhuguo Ma
Institute of Atmospheric Physics Chinese Academy of Sciences

Jianping Duan
Institute of Atmospheric Physics Chinese Academy of Sciences

Danqiong Dai
Institute of Atmospheric Physics Chinese Academy of Sciences

Haoxin Zhang
Institute of Atmospheric Physics Chinese Academy of Sciences

Research Article

Keywords: Land–atmosphere coupling, Surface exchange coefficient, Canopy-height27 dependent Czil, Surface fluxes, Climate zones

Posted Date: May 10th, 2021

DOI: https://doi.org/10.21203/rs.3.rs-221209/v1

Version of Record: A version of this preprint was published at Climate Dynamics on January 8th, 2022. See the published version at https://doi.org/10.1007/s00382-021-06129-5.

Effects of surface coupling strength in WRF/Noah-MP model on regional climate simulations over China

Xia Zhang[1,2], Liang Chen[1,*], Zhuguo Ma[1,2], Jianping Duan[1], Danqiong Dai[1,2] and Haoxin Zhang[1,2]

[1]Key Laboratory of Regional Climate-Environment Research for Temperate East Asia, Institute of Atmospheric Physics, Chinese Academy of Sciences, Beijing, China

[2]University of Chinese Academy of Sciences, Beijing, China

[*]Corresponding author: Liang Chen

Email: chenliang@tea.ac.cn

Tel: 86-10-82995394

Address: Huayanli 40#, Chaoyang District, Beijing 100029, China

Abstract

Land–atmosphere energy and moisture exchange can strongly influence local and regional climate. However, high uncertainty exits in the representation of land–atmosphere interactions in numerical models. The parameterization of surface exchange process is greatly affected by varying the parameter C_{zil} which, however, is typically set to a domain-wide constant value. In this study, we examine the sensitivity of regional climate simulations over China to different surface exchange strengths using three C_{zil} schemes (default without C_{zil}, constant $C_{zil} = 0.1$, and dynamic canopy-height-dependent C_{zil}-h schemes) in the 13-km-resolution Weather Research and Forecasting model coupled with a Noah land surface model with multi-parameterization options (WRF/Noah-MP). Our results demonstrate that the C_{zil}-h scheme substantially reduces the overestimations of land–atmosphere coupling strength in the other two schemes, and comparisons with the ChinaFLUX observations indicate the capability of the C_{zil}-h scheme to better match the observed surface energy and water variations. The results of the C_{zil} schemes applying to four typical climate zones of China present that the C_{zil}-h simulations are in the closest agreements with the field observations. The C_{zil}-h scheme can narrow the positive discrepancies of simulated precipitation and surface fluxes as well as the negative biases of T_s in areas of Northeast, North China, Eastern Northwest, and Southwest. Especially, the above remarkable improvements produced by the C_{zil}-h scheme are primarily over areas covering short vegetation. Also noted that the precipitation simulated by the C_{zil}-h scheme exhibits more intricate and unclear changes compared with surface fluxes simulations due to the non-local impacts of surface exchange strength resulted from the fluidity of the atmosphere. Overall, our findings highlight the applicability of the dynamical C_{zil} as a better physical alternative to treat the surface exchange process in atmosphere coupling models.

Keywords: Land–atmosphere coupling; Surface exchange coefficient; Canopy-height-dependent C_{zil}; Surface fluxes; Climate zones

1 Introduction

Land–surface processes, through controlling energy, momentum, and mass transportation to lower atmosphere and then affecting local planetary boundary layer profiles and differential surface heating (Betts et al. 1996; Los et al. 2006), may play a significant role in cloud formation and precipitation generation (Findell and Eltahir 2003; Trier et al. 2004). The influences of local land surface characteristics such as land use, soil, and topography on the occurrence and development of precipitation are manifest especially over strongly land–atmosphere coupled regions (Houze 2012; Koster et al. 2003, 2004; Li et al. 2017; Pielke et al. 2001). For example, previous studies of the midwestern U.S. drought in 1988 and flood in 1993, suggested that the soil moisture condition helps to sustain the extreme circumstances throughout the summer (Atlas et al. 1993; Trenberth and Guillemot 1996). These studies underline that land–atmosphere interactions may hold the key for the improvements of weather forecast and climate prediction.

The land–atmosphere coupling issue was investigated in many observational and modeling studies, such as the calculation of land–atmosphere feedback numbers based on atmospheric moisture budget (Trenberth 1999), the diagnosis of a multi-model integrated coupling coefficient (Koster et al. 2004), and the assessment of the relationship between soil moisture, evaporation, and precipitation (Dirmeyer et al. 2006; Ruiz-Barradas and Nigam 2005; Zhang et al. 2008). However, there are still great uncertainties due to the complexity of coupling process and its strong dependence on model or reanalysis results (Koster et al. 2003, 2004; Seneviratne et al. 2010). For instance, some regions identified as areas of strong coupling between summer rainfall and soil moisture (Koster et al. 2004), however, due to the reliability on the performance of land surface models (LSMs) in predicting coupling strength, could not be correctly captured in the Global Land–atmosphere Coupling Experiment study (Dirmeyer et al. 2006), or even not appear as strong coupling regions such as the central United States (Zhang et al. 2008). Additionally, Ruiz-Barradas and Nigam (2005) demonstrated that excessively land–atmosphere coupling in numerical models produces too much latent heat flux (LH), resulting in potentially incorrect feedback between soil moisture and

precipitation. Therefore, the coupling issue regarding the exchange efficiencies of energy and moisture between land surface and atmosphere, quantified as a parameter C_h (surface exchange coefficient) in numerical models, may potentially constitute a major uncertainty affecting model performance, but theoretical C_h parameterization still remains poorly understood.

During recent decades, there are many theoretical and experimental studies on C_h parameterization in which many efforts have been put into the treatment for the surface roughness lengths of heat or moisture (Z_{ot}) and momentum (Z_{om}) (Brutsaert 1982; Chen et al. 1997; Chen and Zhang 2009; Yang et al. 2008). The roughness lengths describe the characteristics of surface fields combining the effects of land cover, orography and airflow, however, the differences in transfer mechanisms, transporting heat or moisture through molecular diffusion and momentum through pressure fluctuation gradients, generate the discrepancies between Z_{ot} and Z_{om} (Reijmer et al. 2004; Rigden et al. 2018). Beljaars and Viterbo (1994) suggested that using a fixed ratio of Z_{ot}/Z_{om} = 10 could contribute to the improvements in simulated surface sensible heat flux (SH) and land surface temperature (T_s). Zilitinkevich (1995) created an empirical coefficient C_{zil} that can bridge the relationship between Z_{ot} and Z_{om}. Chen et al. (1997) recommended using the Zilitinkevich formula with C_{zil} = 0.1 which yields the results similar in most cases to the use of Z_{ot}/Z_{om} = 10, but the former non-fixed formulation is physically more preferable and helps reduce forecast precipitation bias; since then, the C_{zil} = 0.1 in Zilitinkevich's formulation has been commonly used in the NCEP operational prediction systems. Further, Chen and Zhang (2009) proposed a vegetation-type dependent C_{zil} which could achieve more realistic application for models in representing land–atmosphere coupling.

Recent studies have been limited to the response of land–surface process to the C_h parameterization, but ignored what extent changing the C_h schemes can really improve the regional climate simulations. The importance of surface roughness in land–surface process impacts on atmosphere has been frequently studied, e.g., the numerical experiments of Maynard and Royer (2004) demonstrated the reduced surface roughness plays a dominant role in African tropical deforestation affecting climate change.

Therefore, it is necessary to explore the sensitivity of climate change to the parameter C_h which heavily relies on surface roughness and directly reflects the strength of land–atmosphere coupling. Additionally, the C_h parameterization with a dynamic C_{zil} has more applications for the evaluation over North America (e.g. Chen and Zhang 2009; Chen et al. 2019; Zheng et al. 2015), but the C_h evaluations in China have been conducted in only few investigations confined to the change of land–surface process and small areas such as at individual arid and semi-arid sites (Chen et al. 2010; Yang et al. 2008) and in Yangtze River basin (Huang et al. 2016). The C_{zil} emperical coefficient contributes most to the uncertainty in the surface energy flux estimates (Siemann et al. 2018), and the specification of the coefficient affects areas of strong land–atmosphere coupling in both the simulated general location and strength (Zheng et al. 2015). Thus, although some investigations regarding the effects of the dynamic C_{zil} on surface flux and precipitation simulations at a point or regional scale (Chen et al. 2010; Huang et al. 2016; Trier et al. 2011) have been conducted, the parameterization of C_h still has large sensitivity and uncertainty to the changes in C_{zil} over regions spanning various topography, land cover, and climate change, especailly for China. Some issues regarding how to properly parameterize coupling strength, and to what extent to affect the simulated surface flux and regional rainfall need to be further explored.

The objective of this study is to assess the variability in regional climate simulations in response to the representation of land–atmosphere coupling in numerical models, and to provide potential mechanisms by which this occurs. Differing from previous studies directly adjusting C_{zil} values in Chen97 scheme (e.g. Chen and Zhang 2009; Huang et al. 2016; Zheng et al. 2015), we introduced the Zilitinkevich formula with a dynamic C_{zil} into the Monin–Obukhov (M–O) scheme (hereafter C_{zil}-h), using the Weather Research and Forecasting model (WRF) coupled with a Noah land surface model with multi-parameterization options (Noah-MP) (WRF/Noah-MP). Section 2 describes detailed land–atmosphere coupling method and the experimental setup using the coupled WRF/Noah-MP model. Section 3 assesses the capability of C_{zil}-h in improving land–atmosphere coupling, and its impacts on the regional climate

simulations. Section 4 discusses the uncertainty of C_{zil}-h scheme in modelling regional climate. Conclusions are drawn in Sect. 5.

2 Methodology, model and data

2.1 Land–atmosphere coupling method

The Noah-MP LSM provides lower boundary layer conditions for the planetary boundary layer scheme in the coupled atmospheric WRF model (Chen et al. 2007; Skamarock et al. 2008), which relies on the surface fluxes of SH and LH (unit: W m^{-2}), determined through the bulk transfer formulas (Garratt 1992),

$$SH = \rho C_p C_h |U|(\theta_s - \theta_a)\,, \tag{1}$$

$$LH = \rho C_e |U|(q_s - q_a)\,, \tag{2}$$

where ρ is the air density (kg m^{-3}), C_p is the air heat capacity (J kg^{-1} K^{-1}), and U is the wind speed (m s^{-1}). θ_a and q_a are the potential temperature (K) and specific humidity (kg kg^{-1}) of air, respectively, and θ_s and q_s are at the surface. C_h (unitless) is the surface exchange coefficient for SH, and C_e is for LH. Many studies (e.g., Högström 1967; Swinbank and Dyer 1967) concluded the general equality of C_e and C_h from the high correlation between the air temperature (T_a) and specific humidity over the evaporating surface, and the approximation has been widely adopted in the numerical models (e.g., Chen et al. 1997; Huang et al. 2016; Trier et al. 2011). Therefore, the study focuses on the parameterization of C_h, which is directly linked to coupling strength and controls the inputs of total energy flux into lower atmosphere. The observed values of C_h can be reconstituted from the measurements of variables contained in the following equation (Chen and Zhang 2009),

$$C_h = \frac{SH}{\rho C_p |U|(\theta_s - \theta_a)}\,. \tag{3}$$

Instruments at stations directly provided SH and U; θ_a was converted from observed T_a adiabatically adjusted for the height above the surface, and θ_s was estimated from upwelling longwave radiation following Stephan Boltzmann relation (Yang et al. 2008); the values of C_p and ρ can be derived from observed T_a, relative humidity, and surface pressure (Allen et al. 1998; Goff 1957).

For the M–O scheme within the Noah-MP LSM, C_h is parameterized as function

of roughness length based on the M–O similarity theory (Brutsaert 1982) as follows,

$$C_h = \frac{k^2}{\left[\ln\left(\frac{Z-d_0}{z_{om}}\right)-\psi_m\left(\frac{Z-d_0}{L}\right)\right]\left[\ln\left(\frac{Z-d_0}{z_{ot}}\right)-\psi_h\left(\frac{Z-d_0}{L}\right)\right]}, \quad (4)$$

$$L = -\frac{\rho C_p u_*^3 T_{ah}}{k \cdot g \cdot SH}, \quad (5)$$

where Z is the height above the surface ground (m), d_0 is the zero-displacement height (m), L is the M–O length (m), and the ratio $(Z-d_0)/L$ is termed as non-dimensional M–O stability parameter ζ. T_{ah} is canopy air temperature (K), u_* is friction velocity (m), k = 0.4 is the von Kaman constant, and g = 9.8 m s^{-2} is the acceleration of gravity. Ψ_m is the stability function for momentum and Ψ_h is for heat (Paulson 1970). Z_{om} is aerodynamic roughness length (m), denoting the height at which the extrapolated wind speed goes to zero. Z_{ot} is thermal roughness length (m), and represents the height at which the extrapolated T_a equals to the T_s.

Z_{ot} through a function of atmospheric flow can be related to Z_{om}, proposed by Zilitinkevich (1995) as,

$$Z_{ot} = Z_{om} \exp\left(-kC_{zil}\sqrt{R_e}\right), \quad R_e = \frac{u^* Z_{om}}{\upsilon}, \quad (6)$$

where C_{zil} is an empirical coefficient, v is the kinematic molecular viscosity (~1.5×10^{-5} m^2 s^{-1}), and R_e is the roughness Reynolds number. The C_{zil} values are usually assumed to be the range of 0.01 to 1.0, with surface coupling varying from strong to weak (Chen et al. 1997; Zheng et al. 2015). The C_{zil} in the current versions of WRF model is assigned as 0.1, based on earlier model comparisons and calibrations with field data (Chen et al. 1997), and only the Chen97 option has access to the default C_{zil} value of 0.1, for the M–O option assumes $Z_{ot} = Z_{om}$ without considering C_{zil}.

Further, a dynamic C_{zil} scheme vegetation type dependent was put forward by Chen and Zhang (2009), and they using the multi-year Ameriflux data and the least squares regression method determined the parameter C_{zil} as a function of canopy height h (unit: m):

$$C_{zil} = 10^{(-0.4h)}. \quad (7)$$

2.2 Coupled WRF/Noah-MP model and experiment design

In this study, the WRF 3.9.1 model coupled with Noah-MP (WRF/Noah-MP) was used

to investigate the sensitivities of regional climate simulations to land–atmosphere coupling. As a state-of-the-art atmospheric modeling system, the WRF model (Skamarock et al. 2008) has full physical process and multiple parameterization options, and thus usually acts as a common framework applied to physical scheme improvement, regional climate simulation, and numerical weather prediction. The Noah-MP LSM (Niu et al. 2011), the successor of the Noah LSM (Chen et al. 1996), is applied as an augmented land surface module in the coupled WRF model. Just like WRF, the selection of multiple physics scheme options is available in the Noah-MP.

The WRF/Noah-MP experiments in this study were initiated at 00:00 UTC on 1 February and ran until 00:00 UTC on 1 September (i.e. vegetation growing season) for the years between 2003 and 2012, in which the first months of each year were treated as the model's spin-up time. As shown in Fig. 1a, the model was integrated over a domain covering the entire China land with a central point at 37°N and 102.5°E. The horizontal resolution was 13 km with grid points of 399 × 344. The grid vertically contained 36 terrain-following eta levels with the model top at 100 hPa. Atmospheric lateral boundary conditions and initial atmospheric fields were taken from the six-hourly 0.75° × 0.75° European Centre for Medium-Range Weather Forecast Interim Reanalysis (ERA-Interim) data (Dee et al. 2011).

The physical parameterization schemes employed in the study include the Noah-MP land-surface model (Niu et al. 2011), the Thompson microphysics (Thompson et al. 2008), Kain-Fritsch convection (Kain 2004), the Yonsei University planetary boundary layer (Hong et al. 2006), and the rapid radiative transfer model (Iacono et al. 2008). The Noah-MP provides two options to calculate C_h: the M–O (Brutsaert 1982) and the Chen97 (Chen et al. 1997) schemes. Both of them are based on the M–O similarity theory, and rely heavily on aerodynamic (Z_{om}) and thermal (Z_{ot}) roughness lengths as well as the atmospheric stability. The primary differences lie on the treatment of roughness lengths, i.e., the Chen97 through the parameter C_{zil} accounts for the discrepancy between Z_{ot} and Z_{om} (usually C_{zil} = 0.1, so Z_{ot}=Z_{om}/10), while the M–O considers identical roughness lengths with the zero-displacement height. In this study, we performed model experiments by incorporating the Z_{ot}/Z_{om} relation of Eq. (6) with

a dynamic C_{zil} of Eq. (7) into the M–O scheme.

Three cases were designed to simulate the different responses of the regional climate simulations to land–atmosphere coupling: Case 1 (Default; C_{zil} ~0) adopted the original M–O option to calculate C_h, Case 2 (Czil; C_{zil} = 0.1) adopted a typical constant C_{zil} value, and Case 3 (Newczil; C_{zil}-h) adopted a dynamic canopy height dependent C_{zil}.

2.3 Validation datasets

The surface meteorological data (V3.0) including over 2000 stations during 2003–2012 operated by China Meteorological Administration (CMA) were utilized in deriving regional C_h observations and verifying the performance of model. The variables involved include hourly precipitation and T_a, as well as T_s, surface wind speed, surface humidity and surface pressure at a 6-hourly interval. Using a Cressman-type interpolation, we horizontally interpolated the on-site observations to the gridded data of 399 × 344, which had the same resolution as the regional climate simulations. The SH data required by calculating the C_h observations were obtained from the monthly 0.0833° FLUXNET-MTE (Model Tree Ensemble) dataset provided by Max Planck Institute for Biogeochemistry. The gridded FLUXNET-MTE dataset was integrated using global 253 FLUXNET eddy covariance observations and the MTE algorithm of machine learning technology (Jung et al. 2009). The FLUXNET-MTE products have been widely employed as a proxy for observations to the analysis of land–atmosphere energy exchanges and the validation of land surface modeling at regional and global scales (Bonan et al. 2011; Gan et al. 2019; Zhang et al. 2019). It should be noted that the gridded dataset has no values in areas of western China for the lack of observation stations, and unevenly distributed flux towers used to train the model tree can create not negligible uncertainty in the product. Additionally, we collected measurements at nine flux tower sites (Table 1) from Chinese terrestrial ecosystem flux research network (ChinaFLUX) to reconstruct C_h and evaluate the simulated surface energy and water variations. The 30-min flux observations were located at areas spanning different land–cover types (grassland, forest, and wetland) and climatic regimes (arid, semi-arid, semi-humid, and wet).

In addition, the atmospheric aridity index (AI), the ratio of annual accumulated precipitation to potential evapotranspiration, was utilized to determine dry and wet climatic regions (Hulme 1996; Middleton and Thomas 1992). The AI values were derived using the monthly 0.5° precipitation and potential evapotranspiration during 1983–2012 in CRU-TS3.23 (Climate Research Unit) dataset from the University of East Anglia. The extreme arid, arid, semi-arid, semi-arid and semi-humid, and humid climate zones are defined according to $0 \leq AI < 0.05$, $0.05 \leq AI < 0.20$, $0.20 \leq AI < 0.50$, $0.50 \leq AI < 0.65$, and $AI \geq 0.65$, respectively.

3 Results

3.1 Model verification

Prior to employing WRF model for exploring the characteristics of land–atmosphere coupling and its influences on local climate, it is necessary to examine the model skill using available field observations. Here, we evaluated the default M–O simulations against on-site observations in terms of T_a and precipitation. Three statistics commonly used to quantify the consistency between model outputs and field observations (e.g., Brovkin et al. 2013; Dai et al. 2019) were adopted: the Pearson correlation coefficient, the mean bias error, and root mean square error.

Figure 2 shows that the patterns of simulated summer T_a and precipitation agree well with that of the observations over China for 2003–2012, with spatial correlations of 0.86 and 0.78, respectively. The simulated T_a can capture the observed large-scale pattern, although colder simulations occur in southwest and warmer values are in northwest China. The modeled precipitation bears a resemblance to the observed pattern of low rainfall amounts in the northwest and large amounts in the southeast, despite overestimated magnitude appears in most areas. Further, the model capacity for simulating the temporal evolutions of T_a and precipitation was assessed in four typical climate regions of China (blue rectangles in Fig. 1b). As exhibited in Fig. 3, the model reproduces well the observed T_a and precipitation variability, and mostly presents significantly positive correlations over 0.8 passing the 95% confidence level. However, the simulations in Northeast, North China, and Southwest present cold biases and in

Eastern Northwest tend to be warmer; additionally, the model generates too much rainfall in the four regions, especially in Southwest with a large positive deviation may owing to the influences of Asian summer monsoon and plateau topography (Song et al. 2010; Wang et al. 2014). Accurately estimating T_a and precipitation has been a challenge, especially, generally overestimated precipitation appears in many atmospheric modeling (Liu et al. 2017; Wang et al. 2015). The accuracy of simulation could be improved through the reduction in errors of model boundary conditions as well as the developments in critical physical parameterizations, e.g., the boundary layer scheme and radiative transfer scheme for simulating T_a (Wang and Zeng 2011; Wang et al. 2015), and cloud microphysical scheme and cumulus scheme for precipitation (Gao et al. 2020; Liu et al. 2017).

In general, the WRF model used in this study exhibits the good performance in reoccurring the features of observed large-scale spatial pattern and temporal evolution, and the verification analyses indicate that using the WRF model to conduct sensitivity experiments can offer helpful information regarding the characteristics of the modification of regional climate in relation to different extents of coupling strength.

3.2 Impacts of C_{zil} on land–atmosphere coupling strength

The C_{zil} schemes adopted in the surface layer parameterization through the exchange efficiencies of land–atmosphere energy and moisture may produce pronounced effects on the evolution of weather and climate systems (Chen and Zhang 2009; LeMone et al. 2008; Trier et al. 2011), thus we first comparatively analyzed the C_h simulated in different C_{zil} experiments basing on field observations, prior to assessing the impacts of land–atmosphere coupling on regional climate.

The C_h observations were calculated from Eq. (3) using surface flux and meteorological measurements. Fig. 4a–c shows general overestimations in most areas of China during 2003–2012 summers compared with the observation-derived C_h. Taking Fig. 4a–c along with Fig. 4d–e, the C_{zil}-h scheme produces generally closest C_h values with the observations, and remarkably reduces the positive C_h bias in the default M–O and $C_{zil} = 0.1$ experiments, which implies the improvements of the application for

the dynamic C_{zil} in representing land–atmosphere coupling. Further, the C_h simulations present evident variability across various vegetation types, as Fig. 4f exhibits, a large increase in C_h from a smoothly sparse vegetated surface with short canopies to a rougher flourishing surface with high canopies occurs as the observations show. Particularly, the C_{zil}-h scheme performs best over areas covering short vegetation (e.g., barren, crop, grass, and shrub) with the smallest mean bias error of 0.37, and exhibits similar behavior of coupling strength modification as the default M–O at grids with tall vegetation (e.g., mixed forest), producing overestimated but reasonable C_h values.

The results in this study are generally consistent with the findings obtained using offline Noah-MP simulations over China (Zhang et al. 2021), as well as using FLUXNET observations and numerical models in North America (Chen and Zhang 2009; Chen et al. 2019). Overall, the C_{zil}-h scheme adopted can help improve the representation of land–atmosphere coupling in atmospheric coupled models, and then influence the transport of land–atmosphere energy and moisture, hence, the next focus of this study will be on to what extent the process affecting surface and atmospheric conditions.

3.3 Impacts of C_{zil} on surface energy and water variations

The land–atmosphere coupling (C_h) represented in the atmospheric model was verified to be improved by the C_{zil}-h scheme in Sect. 3.2, further, the potential skill of the C_{zil}-h scheme in replicating the observed surface energy and water components was evaluated. Figure 5 shows the daily evolutions of SH, LH, soil temperature (ST), and SM averaged from the ChinaFLUX grassland sites (Dan, Sw2, Cng, HaM, and Du2; Table 1) and forest sites (Qia, Din, and Cha) during March to August. The ST and SM were simulated in four soil layers (0–0.1, 0.1–0.4, 0.4–1, and 1–2 m), and the observed values were measured at 0.05 m except at Ha2 site of 0.1 m and Sw2 site of 0–0.3 m. The simulated ST and SM were aggregated to match the observed soil layer. The model shows the ability to favorably capture the daily variability of the observed surface energy and water fluxes. However, the values of SH, LH, ST, and SM are generally overestimated by all C_{zil} experiments. By contrast, the simulations from the C_{zil}-h scheme agree better

with the measurements of ChinaFLUX grassland sites, with minimum root mean square errors for SH, LH, and ST of 14.55 W m^{-2}, 18.38 W m^{-2}, and 1.41 °C, respectively. The C_{zil} schemes produce minor differences in the simulated SM. Further, diurnal surface heat fluxes at ChinaFLUX grassland and forest sites are exhibited in Fig. 6. The C_{zil} schemes simulate larger diurnal amplitudes of SH and LH than the flux measurements, especially during the daytime. However, the C_{zil}-*h* scheme substantially reduces the overestimated SH by the default M–O and $C_{zil} = 0.1$ schemes, which corresponds to the behavior of the C_{zil}-*h* scheme in weakening the excessively strong coupling (Fig. 4). Comparatively, the modeled LH values by three C_{zil} schemes show negligible discrepancies for both grassland and forest.

3.4 Responses of regional climate simulations to C_{zil} over four typical climate zones of China

Thus far, we have shown that the C_{zil}-*h* scheme contributes significantly to the improved performance of the WRF/Noah-MP model in representing land–atmosphere coupling and regenerating surface fluxes. Further, the C_{zil}-*h* scheme was applied to four typical climate zones of China (blue rectangles in Fig. 1b), and its behavior in replicating observed regional climate was assessed. Northeast, North China, and Eastern Northwest were located in the dry-wet transition zones that have strong land–atmosphere interactions (Huang et al. 2017; Li et al. 2017; Ma and Fu 2003) and predominately covered with short vegetation (e.g., crop and grass), and the Southwest region located in a humid zone was also chosen primarily because of the large coverage of tall vegetation (e.g., mixed forest).

Figure 7 displays the differences of summertime precipitation between the simulations using three C_{zil} schemes and the CMA field observations during 2003–2012. Different C_{zil} schemes produce generally similar spatial patterns of climatological precipitation, but differ in the precipitation intensity. The simulated precipitation magnitudes are larger than the observations, whereas the C_{zil}-*h* scheme decreases the positive deviations in the other two C_{zil} simulations and provides noticeable improvements in the northeastern of Northeast, the south of North China, the southwest

of Eastern Northwest, and the northeastern of Southwest. Likewise, the C_{zil}-h scheme reduces the negative bias of T_s produced by the default M–O and C_{zil} = 0.1 experiments (Fig. 8), and has the minimal mean deviations from the observations of –3.04 °C, –1.29 °C and –4.18 °C for Northeast, North China and Southwest, respectively. Figures 9–10 show the discrepancies in SH and LH between the WRF/Noah-MP simulations and the FLUXNET-MTE observations. The C_{zil}-h scheme generally narrows the mean biases of surface fluxes simulated by the other two C_{zil} schemes, and presents more consistence with the observations. These features correspond to the skill of the C_{zil}-h scheme to significantly reduce the overestimated C_h by the default M–O and C_{zil} = 0.1 schemes (Fig. 4). The C_{zil}-h scheme through mitigating the efficiency of land–surface coupling (Fig. 4) transfers less surface fluxes into atmosphere (Figs. 9–10), and leads to a corresponding increase in T_s (Fig. 8), which consequently through atmospheric planetary boundary layer affects atmospheric precipitation (Fig. 7). Also note that remarkable improvements in the four climate zones primarily occur in the short vegetation areas with canopy height < 5 m (Fig. 1a).

Atmospheric circulations that affect precipitation were analyzed through moisture flux (i.e., the multification of vector wind and specific humidity) vertically integrated from 1000 to 300 hPa (Fig. 11). The treatment of C_{zil} in the surface layer parameterization has conspicuous effects on the magnitude and direction of horizontal water vapor transport. The differences between the C_{zil} simulations exhibit distinct seasonality and regionality, which appears to be more remarkable deviations in summer and stronger water vapor transport over eastern China. Additionally, atmospheric convective conditions in terms of convective available potential energy (CAPE), planetary boundary layer height (PBLH), and 2-m specific humidity (Fig. 12) were analyzed to reveal the potential influence of convective activity on precipitation using different C_{zil} schemes. CAPE represents the amount of energy available for convection, and is an indicator of atmospheric instability. Compared with the default M–O and C_{zil} = 0.1 schemes, the C_{zil}-h scheme considerably decreases atmospheric instability energy over a wide area, which is unfavorable for the onset of convective triggering and the occurrence of precipitation. The elevated PBLH simulated by the C_{zil}-h scheme

enhances the mixing of water vapor in lower atmosphere, along with more water vapor evaporated by warmer T_s (Fig. 8), leading to a conspicuous reduction in near-surface humidity. These unfavorable convective conditions might potentially reduce the precipitation intensity in the C_{zil}-h experiments over the four climate zones.

Further, to comprehensively understand the physical mechanisms of the change in precipitation induced by the C_{zil}-h scheme, Table 2 quantitatively analyzes the differences in simulations between C_{zil} schemes in the four climate zones through considering thermal and dynamical factors together. The C_{zil}-h scheme simulates less precipitation than the default M–O scheme for Northeast, North China, Eastern Northwest, and Southwest in summer. The decrease in precipitation is associated with less water vapor horizontally transported from moisture source areas such as the Bay of Bengal and the South China Sea (Table 2 and Fig. 11), less water vapor evaporated from drier surface vertically weakening LH, along with lower CAPE stabilizing lower atmosphere and suppressing thermal convection. The SH values decrease concurrently with reduced coupling strength (C_h; Fig. 4) in the C_{zil}-h experiments, leading to a corresponding rise in land–air temperature contrast (ΔT) and hence deepened PBLH. The C_{zil}-h scheme generates intensified precipitation in spring, which corresponds to more water vapor available for precipitation from enhanced horizontal moisture transport, wetter humidity and increased LH under favorable convective conditions. In comparison with the $C_{zil} = 0.1$ simulations, the C_{zil}-h scheme produces less precipitation for the four regions in summer as well as Northeast and Southwest in spring, and increased amount for North China and Eastern Northwest in spring. The responses of the changes in precipitation to the surface and atmosphere components simulated by the C_{zil}-h against the $C_{zil} = 0.1$ scheme are generally consistent with that against the default M–O scheme.

Additionally, according to Table 2, the large discrepancies in ΔT between the C_{zil} simulations primarily arise from the contribution of T_s, and T_a values vary little with different C_{zil} schemes. For example, the difference of summer ΔT in North China between the C_{zil}-h and default M–O schemes is 1.48 °C, in which the mean bias for T_s is 1.28 °C (the contribution of 86.49%) and for T_a is –0.20 °C. These demonstrate the

important role of C_h in controlling T_s, and Yang et al. (2011) indicated that C_h is the most important factor of modeling T_s, thus, considerable efforts by the LSMs modelers have been spent to improve the performance of model in reproducing T_s through the C_h parameterization (Chen et al. 2011; Gomez et al. 2020).

4 Discussions

4.1 Sensitivities of surface flux and precipitation simulations to the C_{zil}-h scheme and the uncertainties of applying the C_{zil}-h scheme

In this study, we have verified that the C_{zil} in the surface layer parameterization can be slightly adjusted by WRF coupled model to improve regional climate simulation over China. Compared with the control experiments without considering C_{zil} or directly setting it as constant 0.1, a dynamic C_{zil} scheme depending on vegetation type (i.e., C_{zil}-h) can achieve improvements in simulating land–atmosphere coupling strength, thus affect atmospheric planetary boundary layer through the exchange of heat and moisture, and then alter regional climate simulations. However, the impacts of the C_{zil}-h scheme on the simulations appear to vary with land–cover types, variables, and seasons, etc. Specifically, the C_{zil}-h scheme has the ability to reduce the overestimations in both the default M–O and C_{zil} = 1 experiments for short vegetation canopies, but it behaves similarly to the default M–O scheme for high canopies, further, such behavior of the C_{zil}-h scheme does not work for all surface and atmospheric variables. Therefore, this section quantifies the sensitivity of simulations to the C_{zil}-h scheme by analyzing the discrepancies between C_{zil} experiments, and discusses the deficiencies of applying the C_{zil}-h scheme in numerical models.

Considering that the experiments designed in this study are greatly affected by land–cover types, we analyze C_h, SH, T_s and precipitation that are strongly influenced by C_{zil} schemes at three dominant vegetation types in China. Figure 13 and Table 3 show the relative deviations between simulations using different C_{zil} schemes. These values are at grassland, cropland, and forest, which were extracted from the areas of Eastern Northwest, North China, and Southwest, respectively (Fig. 1). The relative deviations in C_h of about –10% (–12%) between the C_{zil}-h and default M–O simulations occur in

grassland (cropland), which doubles (quadruples) the amount in that between the C_{zil}-h and the C_{zil} = 0.1 schemes. These indicate the marked influence of C_{zil} coupling coefficient on the simulations and the substantial reduction by the C_{zil}-h scheme in the C_h overestimation by the default M–O scheme, corresponding to the results in Fig. 4. The C_{zil}-h scheme generates an average relative deviation of –8.12% in C_h compared with the control experiments for short vegetation canopies, and the weakened coupling strength results in less surface SH (an average relative deviation of –6.82%) inputs into the atmosphere and a higher T_s (an average relative deviation of 5.28%). The C_h simulations in the C_{zil}-h experiments at forest exhibit large positive deviations (relative deviation > 36%) against the C_{zil} = 0.1 simulations, with consequences for a significantly higher SH (16%) and negative T_s deviation (8%). The precipitation generated by the C_{zil}-h scheme in grassland and cropland produces a mean negative deviation of –4.69% against the control experiments. Although the C_h values simulated by the C_{zil}-h scheme in forest have small negative deviations (< 0.2%) against the default M–O scheme, such minor biases in land–atmosphere coupling strength still result in distinctively different precipitation, especially in summer, with the relative deviations of up to 60%. This arises probably because local available moisture and energy are affected by the enhancement in land–atmosphere exchange efficiency as vegetation grows luxuriantly from spring to summer (Chen and Zhang 2009; Zhang et al., 2021) as well as the influence of horizontal moisture fluxes transport (Fig. 11).

Theoretically speaking, the fundamental reason for the differences in simulations between C_{zil} schemes lies in that, the C_{zil}-h scheme can directly relate surface coupling strength to terrestrial ecosystem through the Eq. (6), thus affecting the ratio of Z_{ot}/Z_{om} that is critical to the C_h calculation. C_{zil} values are assigned according to various vegetation types, with reducing C_{zil} as canopy height increases, and larger C_h through enhancing the efficiencies of energy and moisture exchange affects atmospheric lower boundary conditions (Chen et al. 2019; Trier et al. 2011; Zheng et al. 2015). The coupling strength of tall vegetation canopies with rougher surfaces is 10 times greater than that of low vegetation (Chen and Zhang 2009), however, C_{zil} value changes little over areas with canopy height > 5 m. For example, the C_{zil} difference between 19–20

m canopy heights is only 1.51 $\times 10^{-8}$, but 0.24 is for that between 1–2 m. A close-to-zero C_{zil} for high vegetation results in equivalent aerodynamic and thermal roughness lengths according to Eqs. (6)–(7), therefore, the C_{zil}-h scheme produces positive deviation similar to the default M–O scheme does.

In fact, there are still many deficiencies in applying the C_{zil}-h scheme to atmospheric coupling model for regional climate simulation. Firstly, regarding the canopy height and Z_{om} that play important roles in the experiments, we adopted the default data within MODIS land cover classification in the model, due to the unavailability of the observations covering China. However, taking Sud and Smith (1985) for an example, they indicated that the decrease of surface roughness from 45 cm to 0.02 cm considerably reduces precipitation in the Sahara desert, and the impact is comparable to that of surface albedo enhancement. Therefore, more accurate data used in the C_{zil}-h scheme will contribute to the improvement of C_h parameterization, and may provide more valuable detailed information. Secondly, the C_{zil}-h scheme improves land–atmosphere coupling strength mainly in short vegetation canopies, and the simulations for high vegetation are similar to that of the default M–O scheme, comparatively, the C_{zil} = 0.1 scheme produces C_h closer to the observed. Therefore, based on extensive evaluations of the C_{zil}-h simulations, it may be necessary to consider how to further improve and optimize the C_{zil}-h scheme in future studies. Additionally, the adjustment of land–surface physical processes can substantially affect climate change (Maynard and Royer 2004; Pielke 2001; Trier et al. 2011), simultaneously, the changes in surface water and energy process can result from land–surface feedbacks to atmospheric anomalies (Findell and Eltahir 2003; Wang and Zeng 2011). Deeply exploring whether the land–atmosphere responses and feedbacks differ from C_{zil} schemes may help to further better understand the impacts of C_{zil} value on the land surface and atmosphere, might contributing to improve the C_{zil}-h scheme.

4.2 Impacts and uncertainties of atmospheric dynamics on the representation of land–atmosphere coupling strength

The representation of land–atmosphere coupling in the WRF/Noah-MP model through

adjusting C_{zil} to vary as vegetation types can be improved and then modify the regional climate simulations (Sect. 3.4). Further, near-surface atmospheric dynamic conditions, by influencing surface roughness elements and aerodynamic properties, interact with the dynamical change of the land–atmosphere coupling strength (C_h) in a complicated approach (Rigden et al. 2018; Zhang et al. 2012). Therefore, this section analyzes how atmospheric dynamics affect C_h and in turn alter climate simulations, and discusses the uncertainties of atmospheric dynamics on land–atmosphere coupling represented in numerical models.

In this study, we referred to Zhang et al. (2012) to construct a dynamic comprehensive variable u^2/u^*, in which, surface wind speed (u) significantly changes the structure and morphology of roughness elements (e.g. plant height and density), and friction velocity (u*) can represent the interaction between near-surface airflow and roughness elements (Rigden et al. 2018; Zilitinkevich et al. 2008). Moreover, the M–O stability parameter ζ (the calculation seen in Sect. 2.1), comprehensively considering thermodynamic influences on atmospheric stability and acting as a determinant in C_h parameterization (Grachev et al. 1998; Yang et al. 2001), was also analyzed. Figure 14 depicts the scatter distributions between C_h and u^2/u^*, ζ and precipitation simulated by the C_{zil}-h scheme, respectively, at grassland, cropland, and forest (the coverage equivalent to that in Sect. 4.1). The correlations between C_h and u^2/u^* are significantly positive ($p < 0.05$) for the three vegetation regions, indicating enhanced effects of airflow movement on surface exchange process. The C_h and u^2/u^* in forest have a larger correlation coefficient of 0.64 than that in grassland and cropland (~0.4), implying that the C_h of high vegetation canopies is more susceptible to atmospheric dynamical conditions. The scatters between C_h and u^2/u^* exhibit obvious discrete at grassland and cropland, whereas at forest the variations of u^2/u^* are more concentrated presumably due to the decrease of surface wind speed resulting from the blocking effect of dense canopy (Maynard et al. 2004; Pielke 2001). Thus, the u^2/u^* in forest (55.98 m s^{-1}) has a lower climatic average than in grassland (90.23 m s^{-1}) and cropland (85.51 m s^{-1}), despite larger C_h values for forest (an average lg C_h of –1.61) than cropland (–2.01) and grassland (–2.08). The C_h along with the change of ζ negatively correlated. The ζ mostly

has negative values, denoting unstable atmospheric stratification ($\zeta < -0.01$), and the greater the value of $|\zeta|$, the stronger the instability, accordingly, the intensified the coupling strength (larger C_h values); as atmosphere becomes stability ($\zeta > 0.01$), C_h tends to decrease and the land–atmosphere coupling strength weakens; $-0.01 < \zeta < 0.01$ denotes near-neutral atmosphere. The atmosphere in forest exhibits the strongest instability with a broader range of $|\zeta|$ between $0–1.5\times10^4$, leading to the most efficient land–atmosphere coupling with the range in lg C_h of –2.6 to –0.8. However, the weakest atmospheric instability occurs in grassland, with sparse values of $|\zeta|$ over 10^4 compared to that in forest and cropland, and thus corresponds to the modest coupling strength. The values of C_h and precipitation are distributed relatively discretely, but still show significant positive correlations ($p < 0.05$). Enhanced coupling strength of larger C_h through the exchange of heat and water is conducive to the increase in precipitation, simultaneously, sufficient rainfall enables vegetation to flourish, and in turn makes the C_h larger by affecting surface roughness (Chen and Zhang 2009; Zhang et al. 2013).

The complicated interactions between atmosphere dynamical conditions and the variability in land–atmosphere coupling strength bring challenges to how to more accurately characterize the land–atmosphere interactions in numerical models. The influences of atmospheric dynamics on land surface are closely connected to not only surface roughness geometry such as plant height and density, but also the dynamical response of vegetation to airflow (e.g. the flexibility of crop and grass), however, the intricate process of dynamic roughness changes affecting C_h has yet been implemented in the current models (Gomez et al. 2020; Zhang et al. 2012; Zilitinkevich et al. 2008). Moreover, the variations in Z_{om}, a key factor influencing C_h parameterization, are manifest due to the strong dependence of vegetation growth on precipitation variability (Zhang et al. 2013), however, the Z_{om} values in this study were determined as a function of only vegetation type, just as most current numerical models have done (e.g., Trier et al. 2011), and thus the introduction of dynamical Z_{om} (e.g., monthly values) in the model may improve the simulations.

5 Conclusions

In this study, we investigated the sensitivity of regional climate simulations over China during 2003–2012 to the parameterized land–atmosphere coupling in the 13-km WRF/Noah-MP model. The surface coupling strength in the model is greatly affected by varying the parameter C_{zil}, which is typically set to a constant, through dynamically adjusting values across land–cover types. Thus, we designed three C_{zil} schemes: the default M–O (C_{zil}~0), constant C_{zil} (set to 0.1) and dynamic canopy-height-dependent C_{zil} (C_{zil}-h), and simulations were compared with the observations from over 2000 meteorological stations and nine ChinaFLUX sites. The main conclusions of this study are summarized as follows.

The remarkable differences in the strength of land–atmosphere coupling can be modeled by three C_{zil} schemes. The default M–O scheme substantially overestimates the observation-derived C_h, and the C_{zil} = 0.1 scheme slightly reduces the positive deviation. In contrast, the C_{zil}-h scheme produces the lowest C_h deviation from the observations for short vegetation canopies (e.g., crop, grass, and shrub), and obtains C_h values similar to that of the default M–O scheme for high canopies (e.g., mixed forest). Additionally, comparisons with the ChinaFLUX observations indicate the capability of the C_{zil}-h scheme to better match the observed surface energy and water variations. In general, using the C_{zil}-h scheme can achieve improved representation of the land–atmosphere coupling in the numerical models.

Adjusting C_{zil} to vary as vegetation types can modulate the exchange efficiencies of land–atmosphere energy and moisture, and subsequently through atmospheric planetary boundary layer alter regional climate simulations. The results of the C_{zil} schemes applying to four typical climate zones of China present that the C_{zil}-h simulations are in the closest agreements with the field observations. The C_{zil}-h scheme narrows the positive discrepancies of simulated precipitation and surface fluxes as well as the negative biases of T_s in areas of Northeast, North China, Eastern Northwest, and Southwest compared to the default M–O and C_{zil} = 0.1 schemes. This arises because the C_{zil}-h scheme through mitigating the efficiency of land–surface coupling transfers less surface fluxes into atmosphere, and leads to a corresponding rise in T_s. The elevated

PBLH simulated by the C_{zil}-h scheme enhances the mixing of water vapor in lower atmosphere, along with more moisture evaporated by warmer T_s, resulting in a conspicuous reduction in near-surface humidity. The decreased precipitation in the C_{zil}-h experiments is associated with less water vapor horizontally transported from moisture source areas, less moisture evaporated from drier surface vertically weakening LH, along with smaller CAPE stabilizing lower atmosphere and suppressing thermal convection.

Although the C_{zil}-h scheme has achieved competitive skill in representing land–atmosphere coupling, the deficiencies and uncertainties in the application of the dynamical scheme in atmospheric coupled models, e.g., the accuracy of canopy height and Z_{om} data, the regional applicability of the scheme, and the dynamical response of vegetation to airflow, require to be further explored and resolved through performing a large number of experiments. These may be helpful in accurately characterizing land–atmosphere coupling and further optimizing the C_h parameterization.

Acknowledgments

This work was funded by the Strategic Priority Research Program of the Chinese Academy of Sciences (grant number: XDA23040104), the National Natural Science Foundation of China (grant number: 41875116), and the National Key Scientific and Technological Infrastructure project "Earth System Science Numerical Simulator Facility" (EarthLab). We acknowledge the use of the meteorological station data provided by the China Meteorological Administration (http://data.cma.cn/), the ChinaFLUX observation data from the FLUXNET network (http://www.fluxdata.org), and the FLUXNET model tree ensembles (MTE) products from the Max Planck Institute for Biogeochemistry (http://www.bgc-jena.mpg.de/geodb/).

Conflicts of interest: There are no conflicts of interest to declare.

References

Allen RG, Pereira LS, Raes D Smith M (1998) Crop evaporation guidelines for computing crop water requirements, FAO-Food and Agriculture Organization of the United Nations. Irrigation and drainage (pp. 56). Rome, Italy.

Atlas R, Wolfson N, Terry J (1993) The effect of SST and soil-moisture anomalies on GLA model simulations of the 1988 united-states summer drought. Journal of Climate 6(11):2034-2048. doi:10.1175/1520-0442(1993)006<2034:teosas>2.0.co;2

Beljaars ACM, Viterbo P (1994) The sensitivity of winter evaporation to the formulation of aerodynamic resistance in the ECMWF model. Boundary-Layer Meteorology 71(1-2):135-149. doi:10.1007/bf00709223

Betts AK, Ball JH, Beljaars ACM, Miller MJ, Viterbo PA (1996) The land surface-atmosphere interaction: A review based on observational and global modeling perspectives. Journal of Geophysical Research: Atmospheres 101(D3):7209-7225. doi:10.1029/95jd02135

Bonan GB et al. (2011) Improving canopy processes in the Community Land Model version 4 (CLM4) using global flux fields empirically inferred from FLUXNET data. Journal of Geophysical Research-Biogeosciences 116:22. doi:10.1029/2010jg001593

Brovkin V, Boysen L, Raddatz T, Gayler V, Loew A, Claussen M (2013) Evaluation of vegetation cover and land-surface albedo in MPI-ESM CMIP5 simulations. Journal of Advances in Modeling Earth Systems 5(1):48-57. doi:10.1029/2012ms000169

Brutsaert WA (1982) Evaporation into the atmosphere: Theory, history and applications (pp. 299). D. Reidel, Dordrecht, Netherlands: Cornell University, USA. https://doi.org/10.1007/978-94-017-1497-6

Chen F, Janjic Z, Mitchell K (1997) Impact of atmospheric surface-layer parameterizations in the new land-surface scheme of the NCEP mesoscale Eta model. Boundary-Layer Meteorology 85(3):391-421. doi:10.1023/a:1000531001463

Chen F et al. (2007) Description and Evaluation of the Characteristics of the NCAR High-Resolution Land Data Assimilation System. Journal of Applied Meteorology and Climatology 46(6):694-713. doi:10.1175/jam2463.1

Chen F, Warner TT, Manning K (2001) Sensitivity of Orographic Moist Convection to Landscape Variability: A Study of the Buffalo Creek, Colorado, Flash Flood Case of 1996. Journal of the Atmospheric Sciences 58(21):3204-3223. doi:10.1175/1520-0469(2001)058<3204:soomct>2.0.co;2

Chen F, Zhang Y (2009) On the coupling strength between the land surface and the atmosphere: From viewpoint of surface exchange coefficients. Geophysical Research Letters 36:5. doi:10.1029/2009gl037980

Chen L, Li YP, Chen F, Barlage M, Zhang Z, Li ZH (2019) Using 4-km WRF CONUS simulations to assess impacts of the surface coupling strength on regional climate simulation. Climate Dynamics 53(9-10):6397-6416. doi:10.1007/s00382-019-04932-9

Chen YY, Yang K, He J, Qin J, Shi JC, Du JY, He Q (2011) Improving land surface temperature modeling for dry land of China. Journal of Geophysical Research-Atmospheres 116:15. doi:10.1029/2011jd015921

Chen YY, Yang K, Zhou DG, Qin J, Guo XF (2010) Improving the NOAH land surface model in arid regions with an appropriate parameterization of the thermal roughness length. Journal of Hydrometeorology 11(4):995-1006. doi:10.1175/2010jhm1185.1

Dai YJ et al. (2019) A global high-resolution data set of soil hydraulic and thermal properties for land surface modeling. Journal of Advances in Modeling Earth Systems 11(9):2996-3023. doi:10.1029/2019ms001784

Dee DP et al. (2011) The ERA-Interim reanalysis: configuration and performance of the data assimilation system. Quarterly Journal of the Royal Meteorological Society 137(656):553-597. doi:10.1002/qj.828

Dirmeyer PA, Koster RD, Guo ZC (2006) Do global models properly represent the feedback between land and atmosphere? Journal of Hydrometeorology 7(6):1177-1198. doi:10.1175/jhm532.1

Findell KL, Eltahir EAB (2003) Atmospheric controls on soil moisture-boundary layer interactions. Part II: Feedbacks within the continental United States. Journal of Hydrometeorology 4(3):570-583. doi:10.1175/1525-7541(2003)004<0570:acosml>2.0.co;2

Gan Y, Liang XZ, Duan Q, Chen F, Li J, Zhang Y (2019) Assessment and reduction of the physical parameterization uncertainty for Noah-MP land surface model. Water Resources Research 55(7):5518-5538. doi:10.1029/2019wr024814

Gao Y, Chen F, Jiang Y (2020) Evaluation of a Convection-Permitting Modeling of Precipitation over the Tibetan Plateau and Its Influences on the Simulation of Snow-Cover Fraction. Journal of Hydrometeorology 21(7):1531-1548. doi:10.1175/jhm-d-19-0277.1

Garratt JR (1992) The atmospheric boundary layer (pp. 316). Cambridge University Press, New York.

Goff JA (1957) Saturation pressure of water on the new Kelvin temperature scale, Transactions of the American Society of Heating and Ventilating Engineers (pp. 347-354). Canada: General Books LLC.

Gomez I, Caselles V, Estrela MJ (2020) Improving RAMS and WRF mesoscale forecasts over two distinct vegetation covers using an appropriate thermal roughness length parameterization. Agricultural and Forest Meteorology 280:11. doi:10.1016/j.agrformet.2019.107791

Grachev AA, Fairall CW, Larsen SE (1998) On the determination of the neutral drag coefficient in the convective boundary layer. Boundary-Layer Meteorology 86(2):257-278. doi:10.1023/a:1000617300732

Högström U (1967) Turbulent water-vapor transfer at different stability conditions. The Physics of Fluids 10(9):S247-S254. doi:10.1063/1.1762460

Hong SY, Noh Y, Dudhia J (2006) A new vertical diffusion package with an explicit treatment of entrainment processes. Monthly Weather Review 134(9):2318-2341. doi:10.1175/mwr3199.1

Houze RA (2012) Orographic effects on precipitating clouds. Reviews of Geophysics 50:47. doi:10.1029/2011rg000365

Huang J et al. (2017) Dryland climate change: Recent progress and challenges. Reviews of Geophysics 55(3):719-778. doi:10.1002/2016rg000550

Huang Y et al. (2016) Effects of roughness length parameterizations on regional-scale land surface modeling of alpine grasslands in the Yangtze river basin. Journal of Hydrometeorology 17(4):1069-1085. doi:10.1175/jhm-d-15-0049.1

Hulme M (1996) Recent climatic change in the World's drylands. Geophysical Research Letters 23(1):61-64. doi:10.1029/95gl03586

Iacono MJ, Delamere JS, Mlawer EJ, Shephard MW, Clough SA, Collins WD (2008) Radiative forcing by long-lived greenhouse gases: Calculations with the AER radiative transfer models. Journal of Geophysical Research-Atmospheres 113(D13):8. doi:10.1029/2008jd009944

Jung M, Reichstein M, Bondeau A (2009) Towards global empirical upscaling of FLUXNET eddy covariance observations: validation of a model tree ensemble approach using a biosphere model. Biogeosciences 6(10):2001-2013. doi:10.5194/bg-6-2001-2009

Kain JS (2004) The Kain-Fritsch convective parameterization: An update. Journal of Applied Meteorology 43(1):170-181. doi:10.1175/1520-0450(2004)043<0170:tkcpau>2.0.co;2

Koster RD et al. (2004) Regions of strong coupling between soil moisture and precipitation. Science 305(5687):1138-1140. doi:10.1126/science.1100217

Koster RD, Suarez MJ, Higgins RW, Van den Dool HM (2003) Observational evidence that soil moisture variations affect precipitation. Geophysical Research Letters 30(5):4. doi:10.1029/2002gl016571

LeMone MA, Tewari M, Chen F, Alfieri JG, Niyogi D (2008) Evaluation of the Noah land surface model using data from a fair-weather IHOP_2002 day with heterogeneous surface fluxes. Monthly Weather Review 136(12):4915-4941. doi:10.1175/2008mwr2354.1

Li MX, Ma ZG, Gu HP, Yang Q, Zheng ZY (2017) Production of a combined land surface data set and its use to assess land-atmosphere coupling in China. Journal of Geophysical Research: Atmospheres 122(2):948-965. doi:https://doi.org/10.1002/2016JD025511

Liu CH et al. (2017) Continental-scale convection-permitting modeling of the current and future climate of North America. Climate Dynamics 49(1-2):71-95. doi:10.1007/s00382-016-3327-9

Los SO, Weedon GP, North PRJ, Kaduk JD, Taylor CM, Cox PM (2006) An observation-based estimate of the strength of rainfall-vegetation interactions in the Sahel. Geophysical Research Letters 33(16):5. doi:10.1029/2006gl027065

Ma Z, Fu C (2003) Interannual characteristics of the surface hydrological variables over the arid and semi-arid areas of northern China. Global and Planetary Change 37(3):189-200. doi:https://doi.org/10.1016/S0921-8181(02)00203-5

Maynard K, Royer JF (2004) Sensitivity of a general circulation model to land surface parameters in African tropical deforestation experiments. Climate Dynamics 22(6-7):555-572. doi:10.1007/s00382-004-0398-9

Middleton NJ, Thomas DS (1992) World atlas of desertification. Edward Arnold.

Niu GY et al. (2011) The community Noah land surface model with multiparameterization options (Noah-MP): 1. Model description and evaluation with local-scale measurements. Journal of Geophysical Research-Atmospheres 116(D12109):1-19. doi:10.1029/2010jd015139

Paulson CA (1970) The mathematical representation of wind speed and temperature profiles in the unstable atmospheric surface layer. Journal of Applied Meteorology 9(6):857-861. doi:10.1175/1520-0450(1970)009<0857:tmrows>2.0.co;2

Pielke RA (2001) Influence of the spatial distribution of vegetation and soils on the prediction of cumulus convective rainfall. Reviews of Geophysics 39(2):151-177. doi:10.1029/1999rg000072

Reijmer CH, Van Meijgaard E, Van Den Broeke MR (2004) Numerical studies with a regional atmospheric climate model based on changes in the roughness length for momentum and heat over Antarctica. Boundary-Layer Meteorology 111(2):313-337. doi:10.1023/B:BOUN.0000016470.23403.ca

Rigden A, Li D, Salvucci G (2018) Dependence of thermal roughness length on friction velocity across land cover types: A synthesis analysis using AmeriFlux data. Agricultural and Forest Meteorology 249:512-519. doi:10.1016/j.agrformet.2017.06.003

Ruiz-Barradas A, Nigam S (2005) Warm season rainfall variability over the US great plains in observations, NCEP and ERA-40 reanalyses, and NCAR and NASA atmospheric model simulations. Journal of Climate 18(11):1808-1830. doi:10.1175/jcli3343.1

Seneviratne SI et al. (2010) Investigating soil moisture-climate interactions in a changing climate: A review. Earth-Science Reviews 99(3-4):125-161. doi:10.1016/j.earscirev.2010.02.004

Siemann AL, Chaney N, Wood EF (2018) Sensitivity and uncertainty of a long-term, high-resolution, global, terrestrial sensible heat flux data set. Journal of Geophysical Research-Atmospheres 123(10):4988-5000. doi:10.1029/2017jd027785

Skamarock WC et al (2008) A description of the advanced research WRF Version 3. NCAR Technical Note NCAR/TN-475 + STR. https ://doi.org/10.5065/D68S4 MVH

Song JH, Kang HS, Byun YH, Hong SY (2010) Effects of the Tibetan Plateau on the Asian summer monsoon: a numerical case study using a regional climate model. International Journal of Climatology 30(5):743-759. doi:10.1002/joc.1906

Sud YC, Smith WE (1985) The influence of surface-roughness of deserts on the July circulation (a numerical study). Boundary-Layer Meteorology 33(1):15-49. doi:10.1007/bf00137034

Swinbank WC, Dyer AJ (1967) An experimental study in micro-meteorology. Quarterly Journal of the Royal Meteorological Society 93(398):494-500. doi:10.1002/qj.49709339808

Thompson G, Field PR, Rasmussen RM, Hall WD (2008) Explicit Forecasts of Winter Precipitation Using an Improved Bulk Microphysics Scheme. Part II: Implementation of a New Snow Parameterization. Monthly Weather Review 136(12):5095-5115. doi:10.1175/2008mwr2387.1

Trenberth KE (1999) Atmospheric moisture recycling: Role of advection and local evaporation. Journal of Climate 12(5):1368-1381. doi:10.1175/1520-0442(1999)012<1368:amrroa>2.0.co;2

Trenberth KE, Guillemot CJ (1996) Physical processes involved in the 1988 drought and 1993 floods in North America. Journal of Climate 9(6):1288-1298. doi:10.1175/1520-0442(1996)009<1288:ppiitd>2.0.co;2

Trier SB, Chen F, Manning KW (2004) A study of convection initiation in a mesoscale model using high-resolution land surface initial conditions. Monthly Weather Review 132(12):2954-2976. doi:10.1175/mwr2839.1

Trier SB, LeMone MA, Chen F, Manning KW (2011) Effects of surface heat and moisture exchange on ARW-WRF warm-season precipitation forecasts over the central United States. Weather and Forecasting 26(1):3-25. doi:10.1175/2010waf2222426.1

Wang AH, Zeng XB (2011) Sensitivities of terrestrial water cycle simulations to the variations of precipitation and air temperature in China. Journal of Geophysical Research-Atmospheres 116:11. doi:10.1029/2010jd014659

Wang J, Feng JM, Yan ZW (2015) Potential sensitivity of warm season precipitation to urbanization extents: Modeling study in Beijing-Tianjin-Hebei urban agglomeration in China. Journal of Geophysical Research-Atmospheres 120(18):9408-9425. doi:10.1002/2015jd023572

Wang ZQ, Duan AM, Wu GX (2014) Time-lagged impact of spring sensible heat over the Tibetan Plateau on the summer rainfall anomaly in East China: case studies using the WRF model. Climate Dynamics 42(11-12):2885-2898. doi:10.1007/s00382-013-1800-2

Yang K et al. (2008) Turbulent flux transfer over bare-soil surfaces: Characteristics and parameterization. Journal of Applied Meteorology and Climatology 47(1):276-290. doi:10.1175/2007jamc1547.1

Yang K, Tamai N, Koike T (2001) Analytical solution of surface layer similarity equations. Journal of Applied Meteorology 40(9):1647-1653. doi:10.1175/1520-0450(2001)040<1647:asosls>2.0.co;2

Yang ZL et al. (2011) The community Noah land surface model with multiparameterization options (Noah-MP): 2. Evaluation over global river basins. Journal of Geophysical Research-Atmospheres 116(D12110):1-16. doi:10.1029/2010jd015140

Zhang JY, Wang WC, Leung LR (2008) Contribution of land-atmosphere coupling to summer climate variability over the contiguous United States. Journal of Geophysical Research-Atmospheres 113:15. doi:10.1029/2008jd010136

Zhang Q, Li H, Zhang L, Yue P, Shi J (2013) Responses of the land-surface process and its parameters over the natural vegetation underlying surface of the middle of Gansu in loess plateau to precipitation fluctuation. Acta Physica Sinica 62(1):522-532. doi: 10.7498/aps.62.019201

Zhang Q, Zeng J, Yao T (2012) Interaction of aerodynamic roughness length and windflow conditions and its parameterization over vegetation surface. Chinese Science Bulletin 57(13):1559-1567. doi:10.1007/s11434-012-5000-y

Zhang X, Chen L, Ma ZG, Gao YH (2021) Assessment of surface exchange coefficients in the Noah-MP land surface model for different land-cover types in China. International Journal of Climatology n/a(n/a):1-22. doi: https://doi.org/10.1002/joc.6981

Zhang X, Li MX, Ma ZG, Yang Q, Lv MX, Clark R (2019) Assessment of an evapotranspiration deficit drought index in relation to impacts on ecosystems. Advances in Atmospheric Sciences 36(11):1273-1287. doi:10.1007/s00376-019-9061-6

Zheng Y, Kumar A, Niyogi D (2015) Impacts of land-atmosphere coupling on regional rainfall and convection. Climate Dynamics 44(9-10):2383-2409. doi:10.1007/s00382-014-2442-8

Zilitinkevich S (1995) Non-local turbulent transport: Pollution dispersion aspects of coherent structure of convective flows. In H. Power, N. Moussiopoulos, & C. A. Brebbia (Eds.), Air pollution III-volume I. Air pollution theory and simulation (pp. 53–60). Southampton, Boston: Computational Mechanics Publications.

Zilitinkevich SS, Mammarella I, Baklanov AA, Joffre SM (2008) The effect of stratification on the aerodynamic roughness length and displacement height. Boundary-Layer Meteorology 129(2):179-190. doi:10.1007/s10546-008-9307-9

Figures

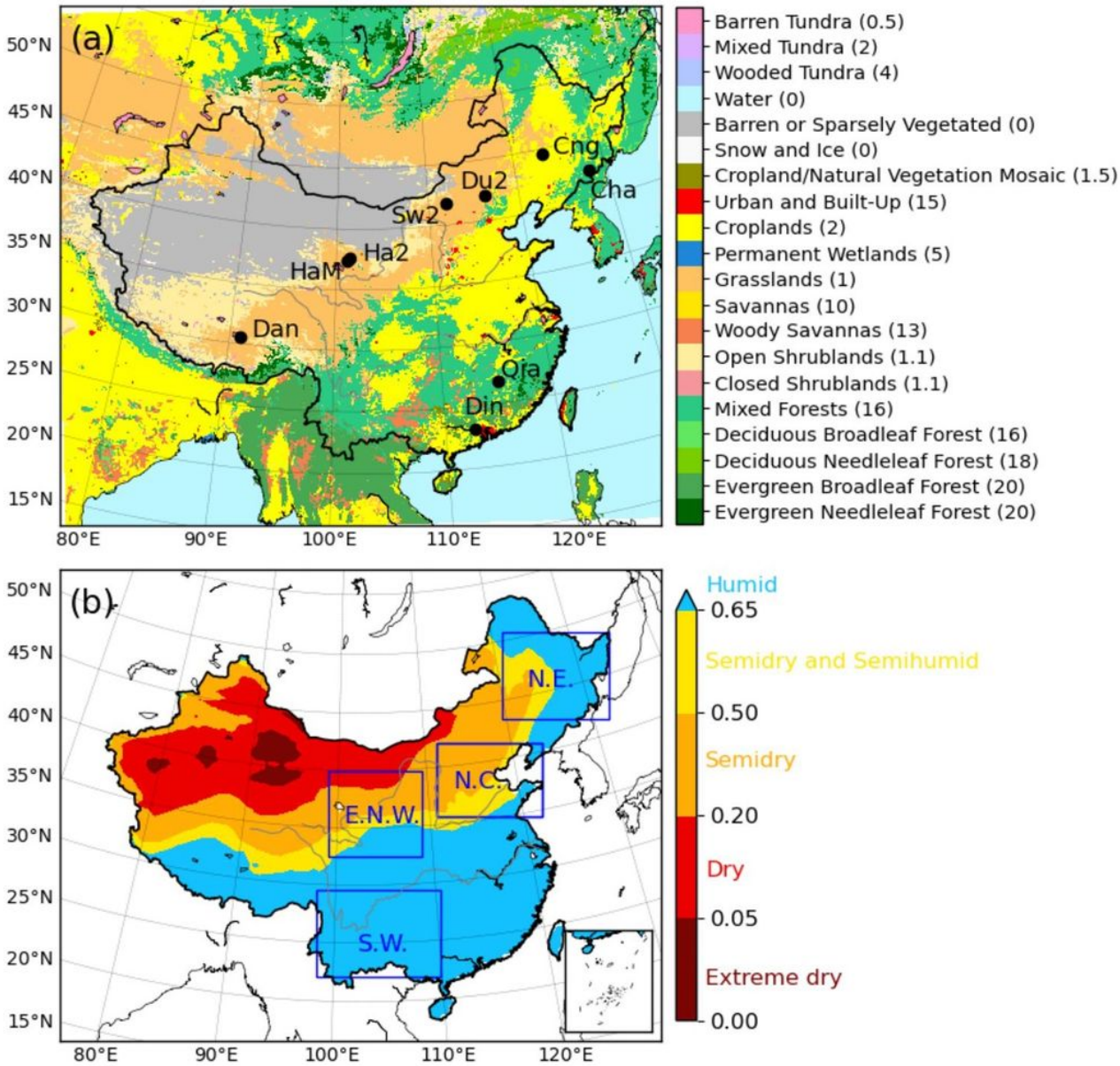

Figure 1

(a) Weather Research and Forecasting model coupled with a Noah land surface model with multi-parameterization options (WRF/Noah-MP) modeling domain. Shaded contours represent Moderate Resolution Imaging Spectroradiometer (MODIS) land cover/land use classification within the International Geosphere-Biosphere Program (IGBP). Values in parentheses indicate canopy height (unit: m). Dark circles denote the locations of nine ChinaFLUX sites: Changbaishan (Cha), Changling (Cng), Dangxiong (Dan), Dinghushan (Din), Duolun (Du2), Haibei Alpine (HaM), Haibei Shrubland (Ha2), Qianyanzhou (Qia), and Siziwang Banner (Sw2). (b) Division of wet and dry climate zones in China.

Shaded contours represent atmospheric aridity index, the ratio of annual accumulated precipitation to potential evapotranspiration. Blue rectangles denote four typical climate regions selected in this study. N.E.: Northeast (120~135°E, 42.5~50°N); N.C.: North China (110~123°E, 35~41°N); E.N.W.: Eastern Northwest (99~109°E, 32.5~40°N); S.W.: Southwest (98~111°E, 22~28°N) Note: The designations employed and the presentation of the material on this map do not imply the expression of any opinion whatsoever on the part of Research Square concerning the legal status of any country, territory, city or area or of its authorities, or concerning the delimitation of its frontiers or boundaries. This map has been provided by the authors.

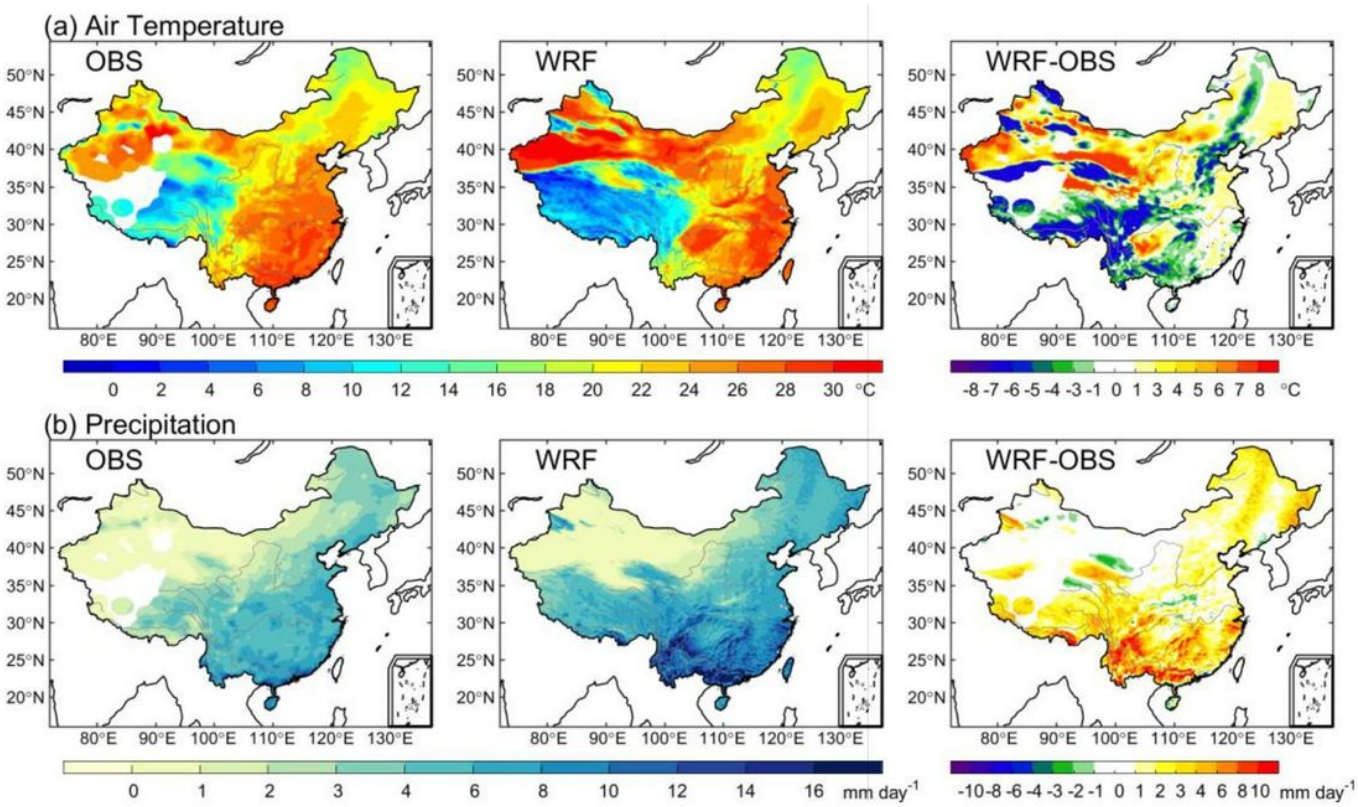

Figure 2

Spatial patterns of (a) air temperature and (b) precipitation in the field observations from China Meteorological Administration (OBS) and the simulations from WRF/Noah-MP model using the default M–O scheme (WRF), as well as their differences (WRF-OBS) during the summers of 2003–2012 Note: The designations employed and the presentation of the material on this map do not imply the expression of any opinion whatsoever on the part of Research Square concerning the legal status of any country, territory, city or area or of its authorities, or concerning the delimitation of its frontiers or boundaries. This map has been provided by the authors.

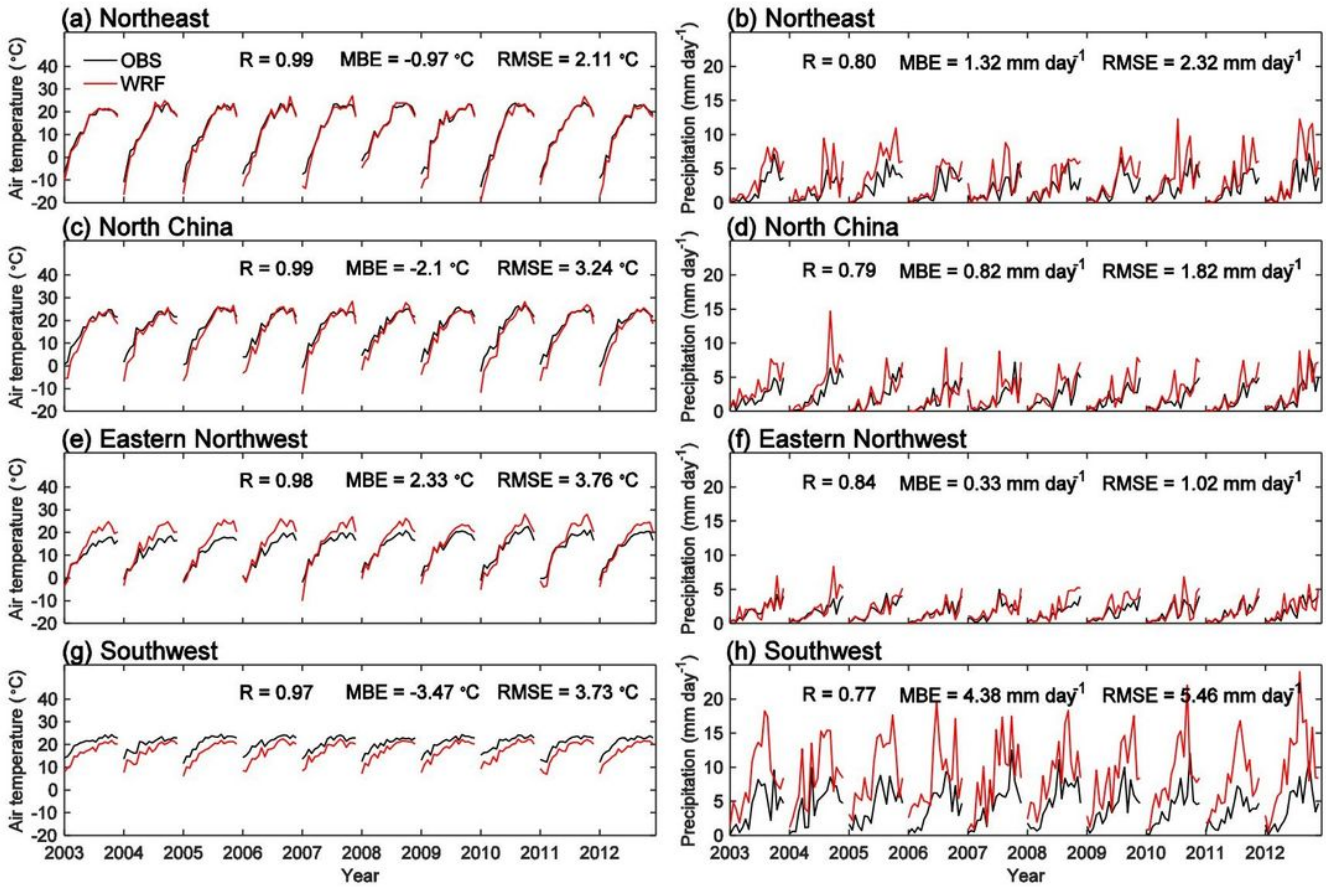

Figure 3

Temporal evolutions of air temperature and precipitation in the field observations from China Meteorological Administration (OBS) and the simulations from WRF/Noah-MP model using the default M–O scheme (WRF) for (a–b) Northeast, (c–d) North China, (e–f) Eastern Northwest and (g–h) Southwest during March to August of 2003–2012. R, MBE, and RMSE denote the Pearson correlation coefficient, the mean bias error, and root mean square error, respectively

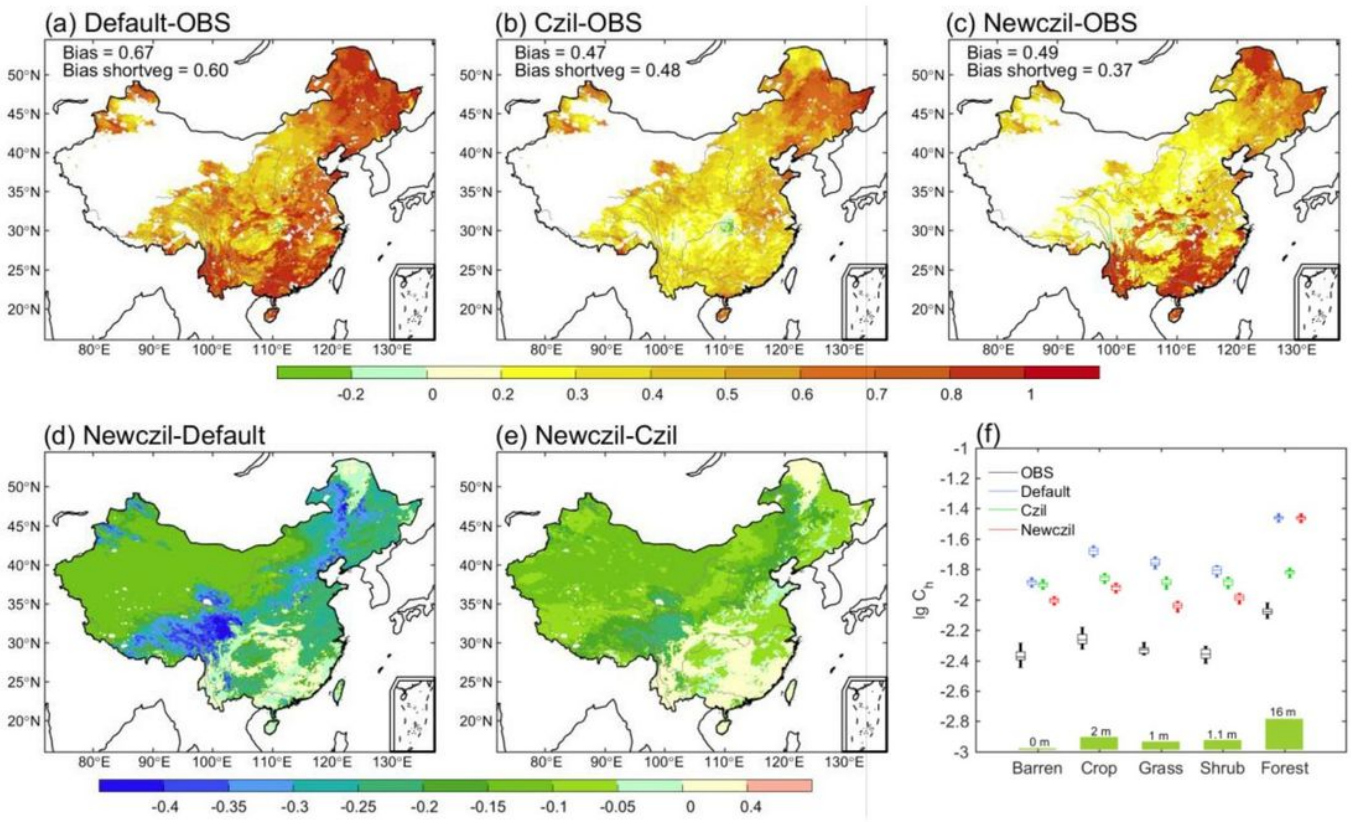

Figure 4

Comparisons of surface exchange coefficient, Ch (plotted at log10 scale), derived from the field observations of China Meteorological Administration (OBS), and calculated by the WRF/Noah-MP model using the default M–O (Default), Czil = 0.1 (Czil), and Czil-h (Newczil) schemes during 2003–2012 summers. (a–c) the differences between the simulations and the observations, (d–e) the differences between the simulations, and (f) regional averaged Ch values for typical land–cover types. Bias: the mean deviation of the simulations from the observations; Bias shortveg: the discrepancy between the simulated and the observed values averaged from short vegetation areas with canopy height < 5 m. Green bars in (f) denote canopy height Note: The designations employed and the presentation of the material on this map do not imply the expression of any opinion whatsoever on the part of Research Square concerning the legal status of any country, territory, city or area or of its authorities, or concerning the delimitation of its frontiers or boundaries. This map has been provided by the authors.

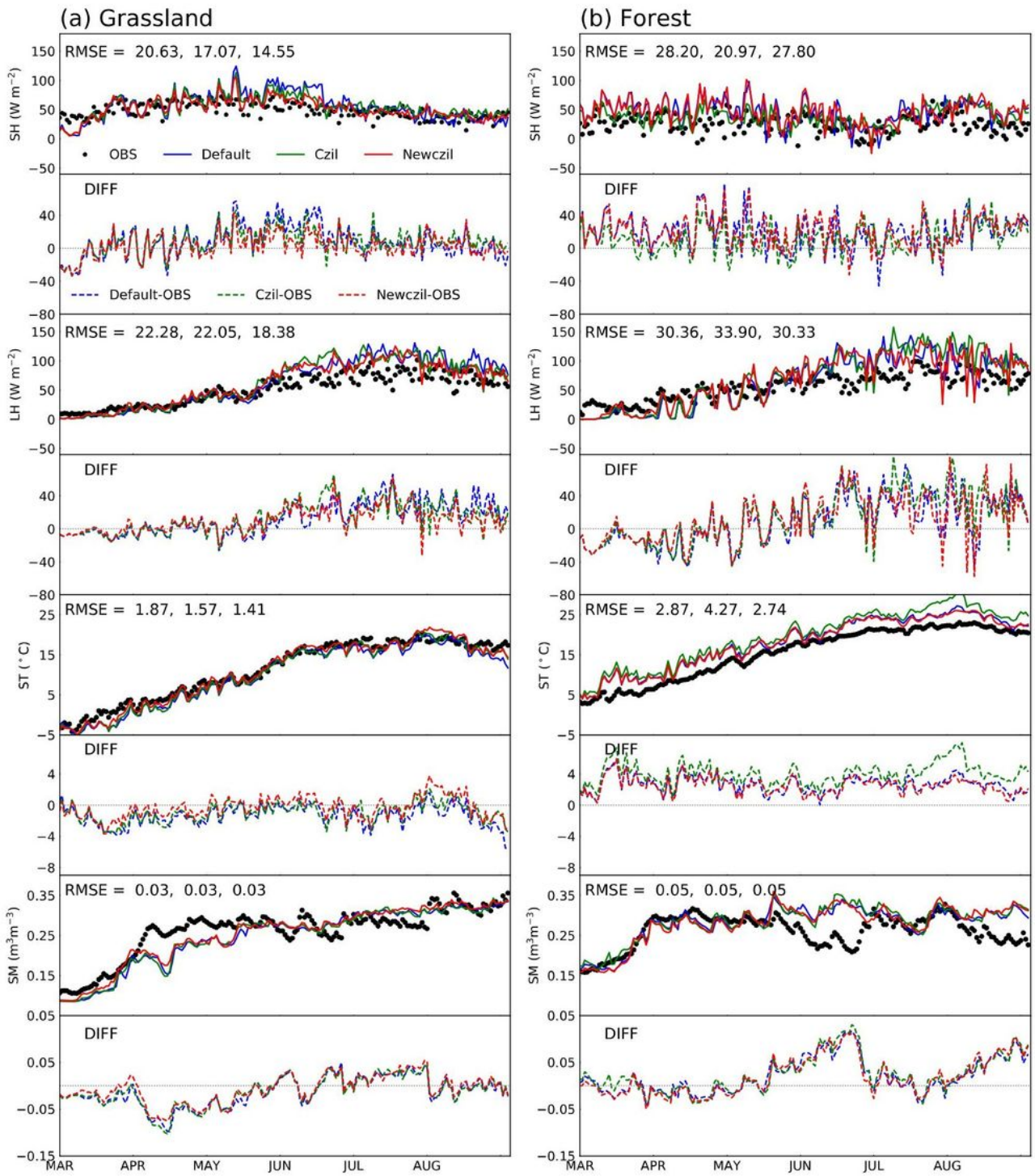

Figure 5

Comparisons of daily sensible heat flux (SH), latent heat flux (LH), soil temperature (ST), and soil moisture (SM) during March to August between the ChinaFLUX observations (OBS) and the WRF/Noah-MP simulations using the default M–O (Default), Czil = 0.1 (Czil), and Czil-h (Newczil) schemes. The values in (a) were averaged from the ChinaFLUX grassland sites (Dan, Sw2, Cng, HaM, and Du2) for respective available years (Table 1), and the values in (b) from the forest sites (Qia, Din, and Cha). Root

mean square errors (RMSE) in sequence for the default M–O, Czil = 0.1, and Czil-h simulations are displayed in each panel

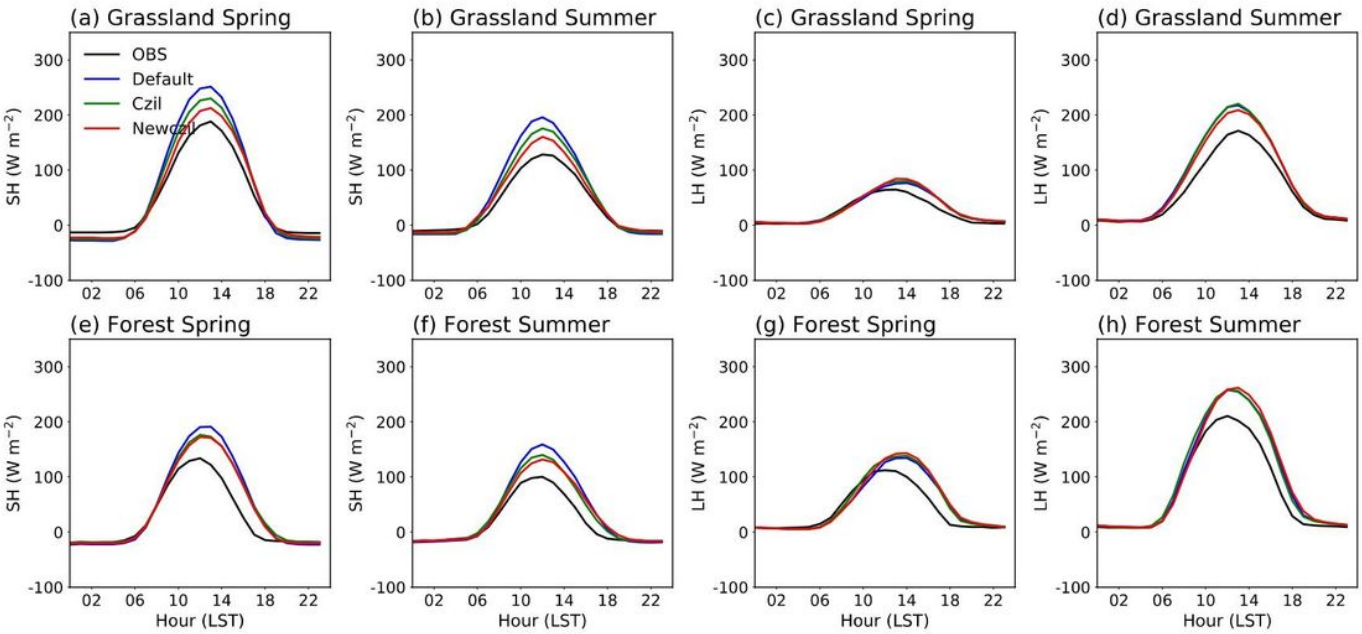

Figure 6

Diurnal comparisons of sensible heat flux (SH) and latent heat flux (LH) between the ChinaFLUX observations (OBS) and the WRF/Noah-MP simulations using the default M–O (Default), Czil = 0.1 (Czil), and Czil-h (Newczil) schemes. The values in (a–d) were averaged from the ChinaFLUX grassland sites (Dan, Sw2, Cng, HaM, and Du2) for respective available years (Table 1), and the values in (e–h) from the forest sites (Qia, Din, and Cha)

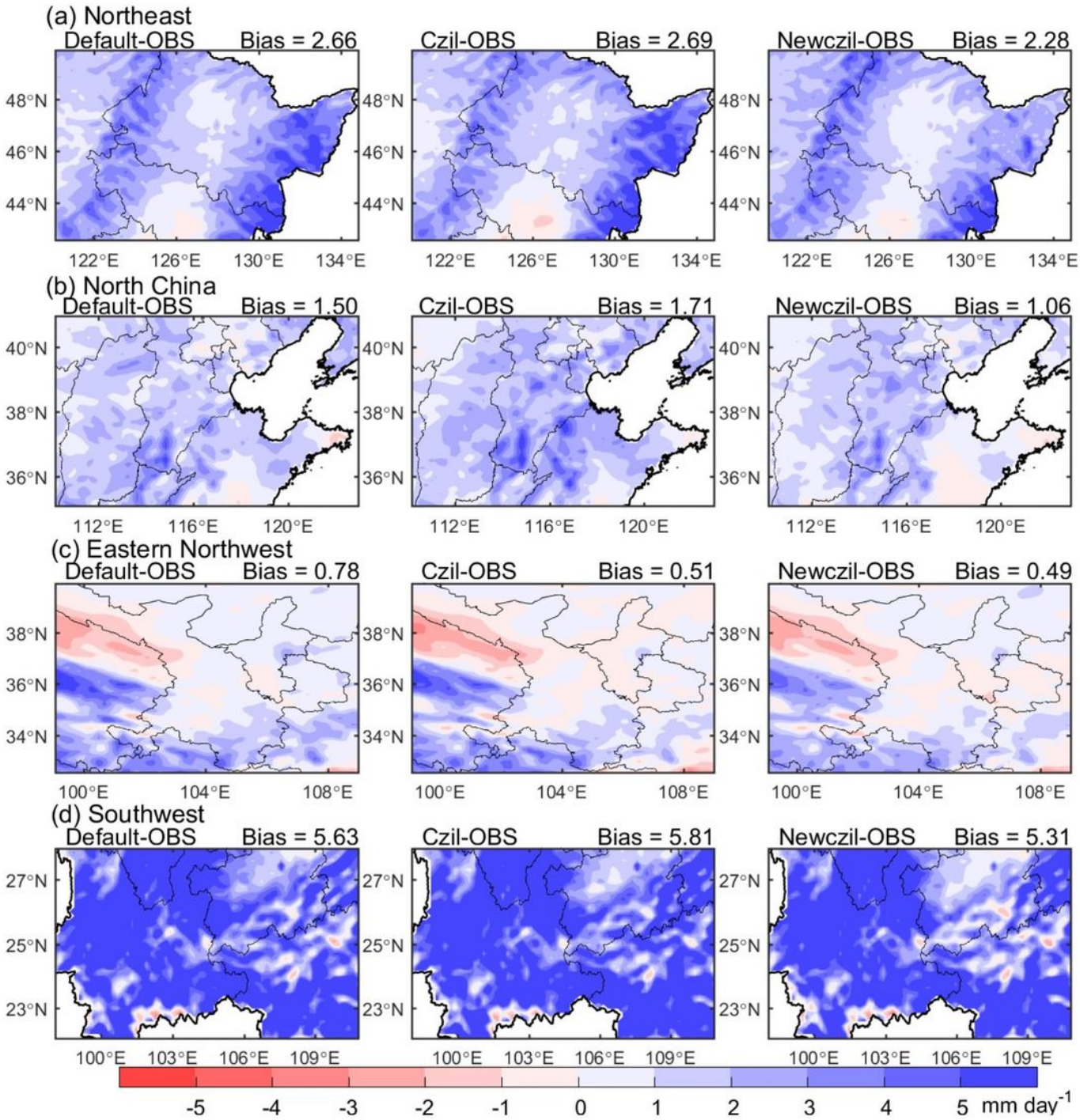

Figure 7

Spatial differences of precipitation between the field observations from China Meteorological Administration (OBS) and the WRF/Noah-MP simulations using the default M–O (Default), Czil = 0.1 (Czil), and Czil-h (Newczil) schemes over (a) Northeast, (b) North China, (c) Eastern Northwest and (d) Southwest during the summers of 2003–2012. Bias: the mean discrepancy between the simulations and the observations Note: The designations employed and the presentation of the material on this map do

not imply the expression of any opinion whatsoever on the part of Research Square concerning the legal status of any country, territory, city or area or of its authorities, or concerning the delimitation of its frontiers or boundaries. This map has been provided by the authors.

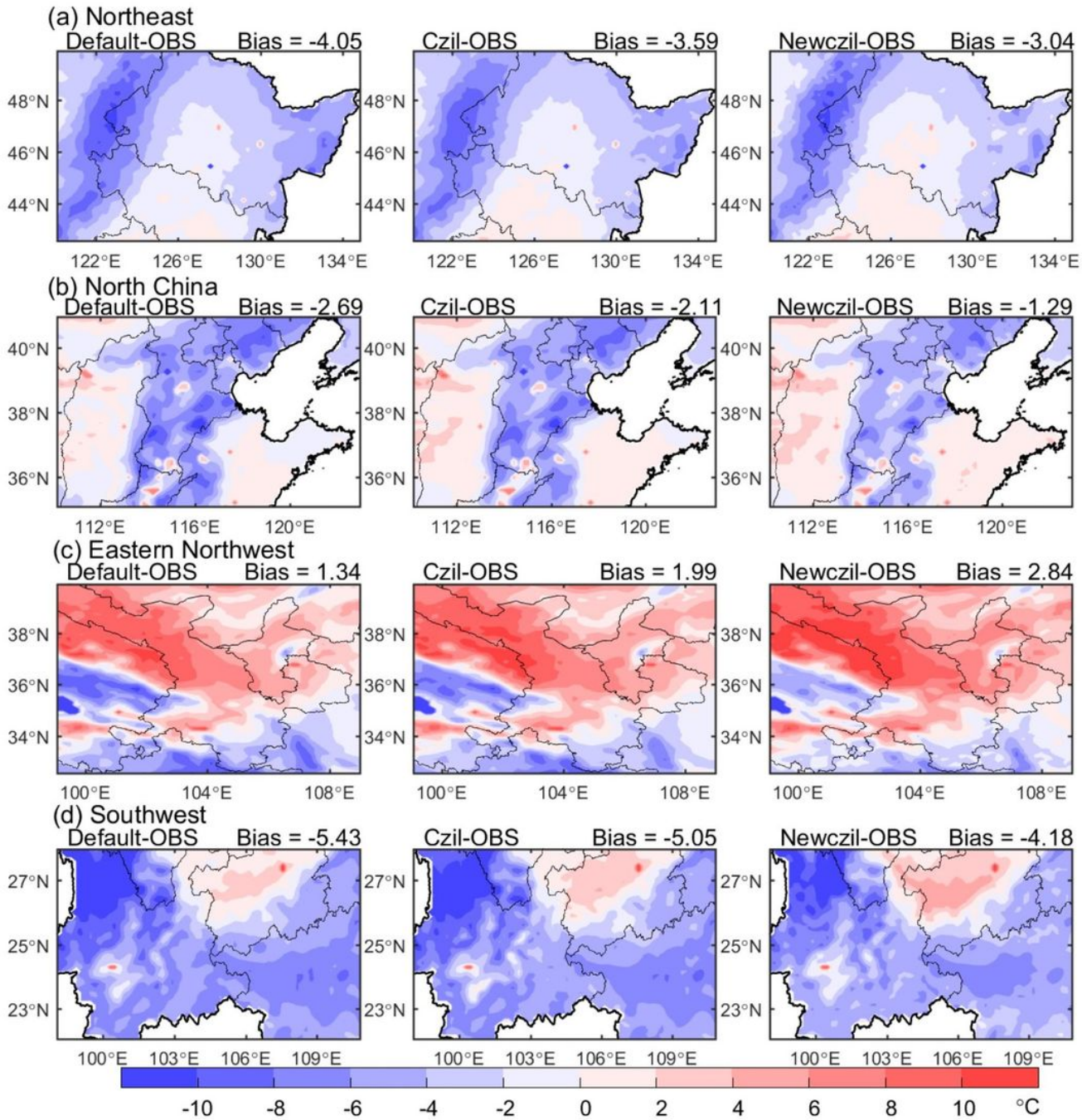

Figure 8

Spatial differences of land surface temperature between the field observations from China Meteorological Administration (OBS) and the WRF/Noah-MP simulations using the default M–O (Default), Czil = 0.1 (Czil), and Czil-h (Newczil) schemes over (a) Northeast, (b) North China, (c) Eastern Northwest and (d) Southwest during the summers of 2003–2012. Bias: the mean discrepancy between the simulations and the observations Note: The designations employed and the presentation of the

material on this map do not imply the expression of any opinion whatsoever on the part of Research Square concerning the legal status of any country, territory, city or area or of its authorities, or concerning the delimitation of its frontiers or boundaries. This map has been provided by the authors.

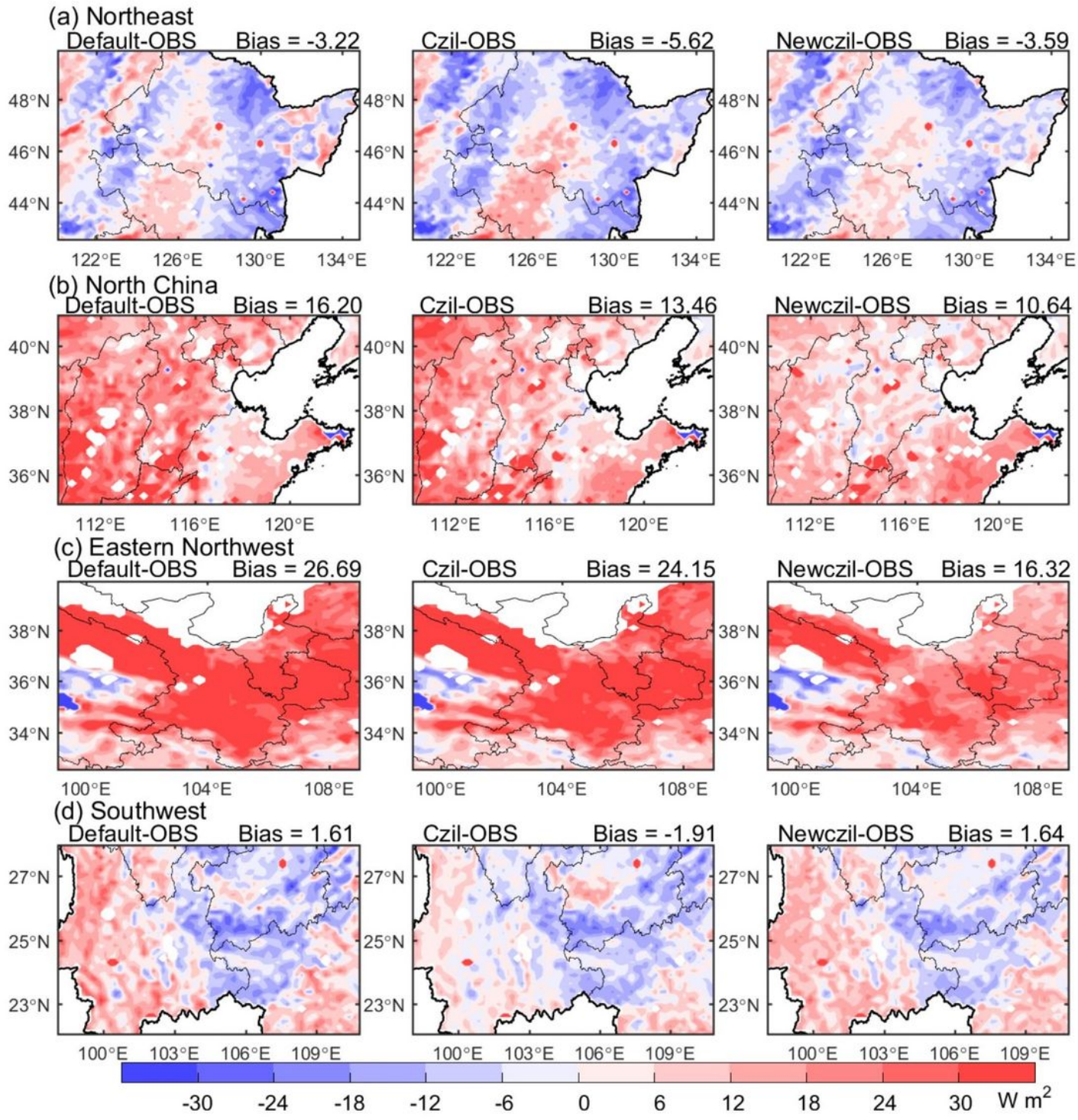

Figure 9

Spatial differences of sensible heat flux between the FLUXNET-MTE observations (OBS) and the WRF/Noah-MP simulations using the default M–O (Default), Czil = 0.1 (Czil), and Czil-h (Newczil)

schemes over (a) Northeast, (b) North China, (c) Eastern Northwest and (d) Southwest during the summers of 2003–2012. Bias: the mean discrepancy between the simulations and the observations Note: The designations employed and the presentation of the material on this map do not imply the expression of any opinion whatsoever on the part of Research Square concerning the legal status of any country, territory, city or area or of its authorities, or concerning the delimitation of its frontiers or boundaries. This map has been provided by the authors.

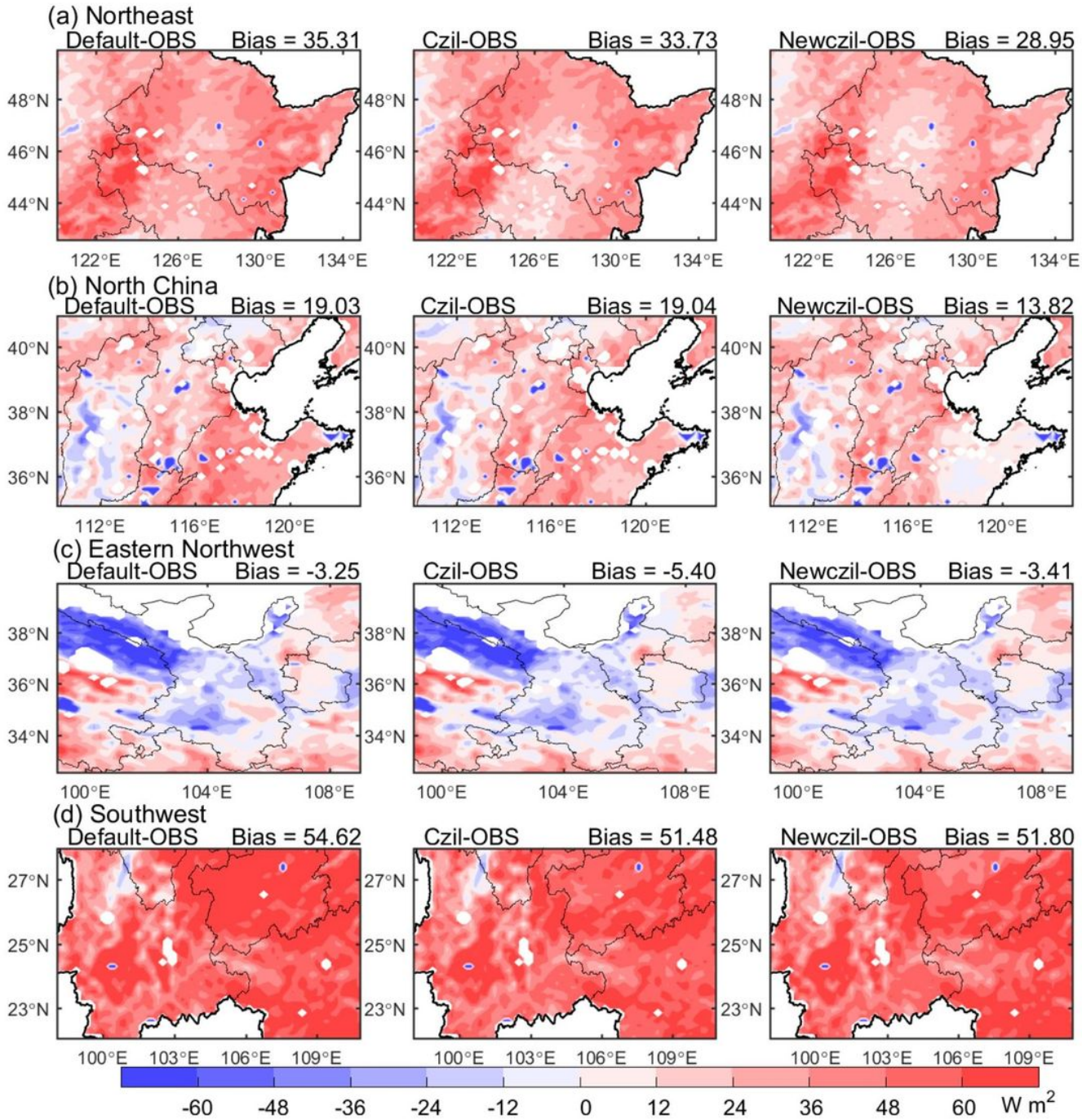

Figure 10

Spatial differences of latent heat flux between the FLUXNET-MTE observations (OBS) and the WRF/Noah-MP simulations using the default M–O (Default), Czil = 0.1 (Czil), and Czil-h (Newczil) schemes over (a) Northeast, (b) North China, (c) Eastern Northwest and (d) Southwest during the summers of 2003–2012. Bias: the mean discrepancy between the simulations and the observations Note: The designations employed and the presentation of the material on this map do not imply the expression of any opinion whatsoever on the part of Research Square concerning the legal status of any country, territory, city or area or of its authorities, or concerning the delimitation of its frontiers or boundaries. This map has been provided by the authors.

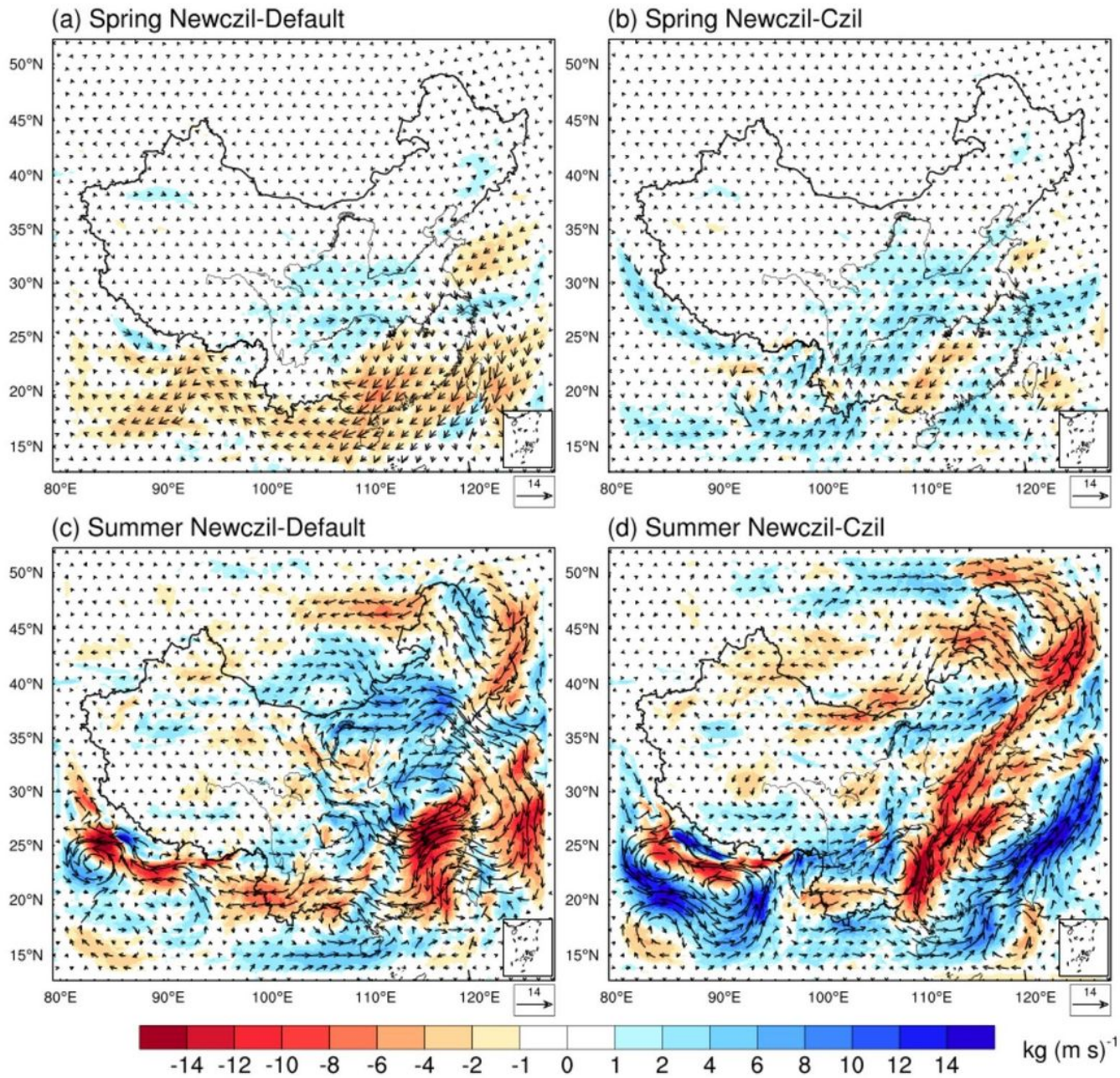

Figure 11

Spatial difference of moisture flux between the simulations using the default M–O (Default), Czil = 0.1 (Czil), and Czil-h (Newczil) schemes during the springs and summers of 2003–2012. The moisture flux values were derived by multiplying specific humidity and vector wind, and vertically integrated from 1000 to 300 hPa Note: The designations employed and the presentation of the material on this map do not imply the expression of any opinion whatsoever on the part of Research Square concerning the legal status of any country, territory, city or area or of its authorities, or concerning the delimitation of its frontiers or boundaries. This map has been provided by the authors.

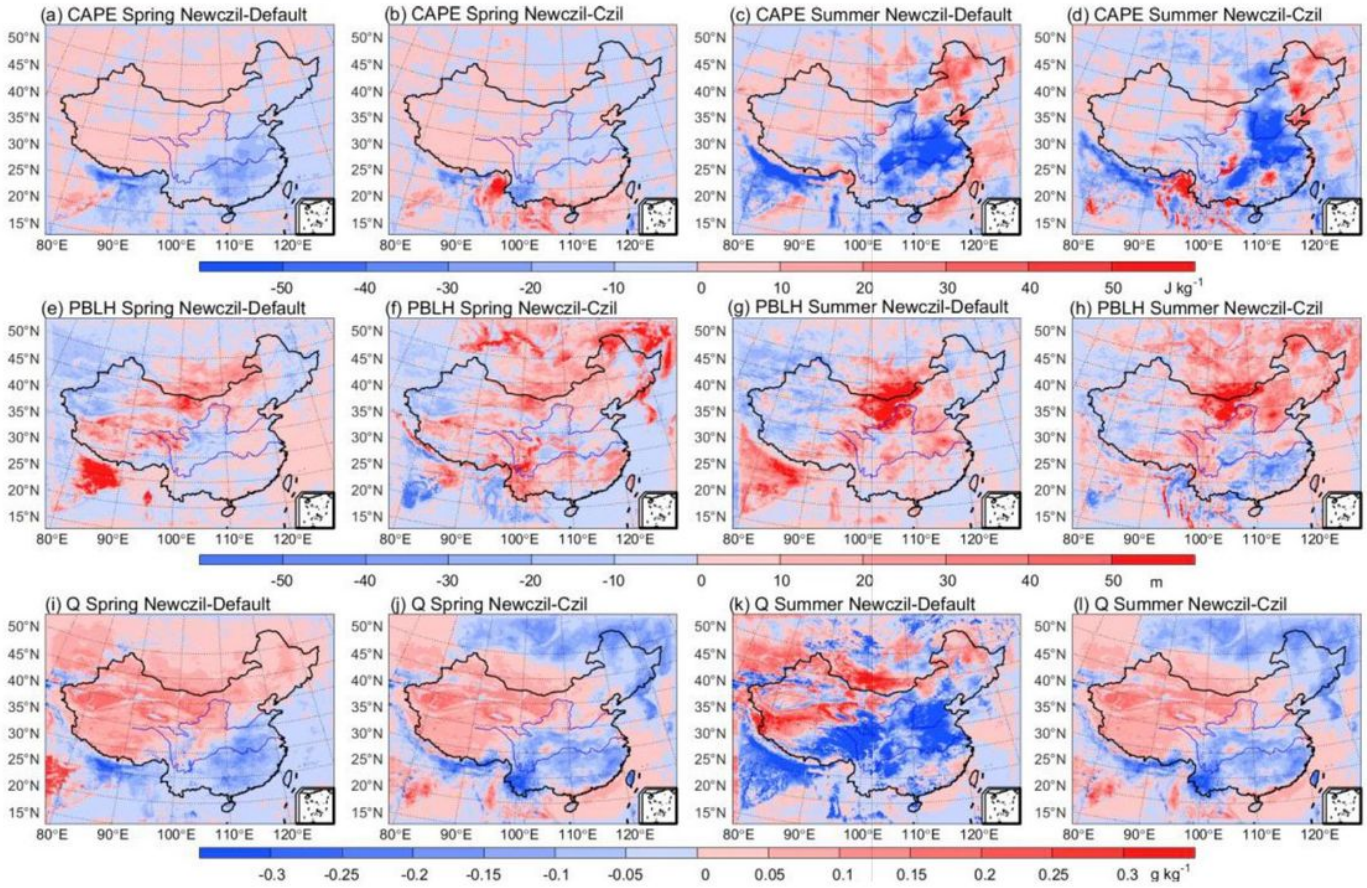

Figure 12

Spatial differences of (a–d) convective available potential energy (CAPE), (e– h) planetary boundary layer height (PBLH), and (i–l) 2-m air specific humidity (Q) between the simulations using the default M–O (Default), Czil = 0.1 (Czil), and Czil-h (Newczil) schemes during the springs and summers of 2003–2012 Note: The designations employed and the presentation of the material on this map do not imply the expression of any opinion whatsoever on the part of Research Square concerning the legal status of any country, territory, city or area or of its authorities, or concerning the delimitation of its frontiers or boundaries. This map has been provided by the authors.

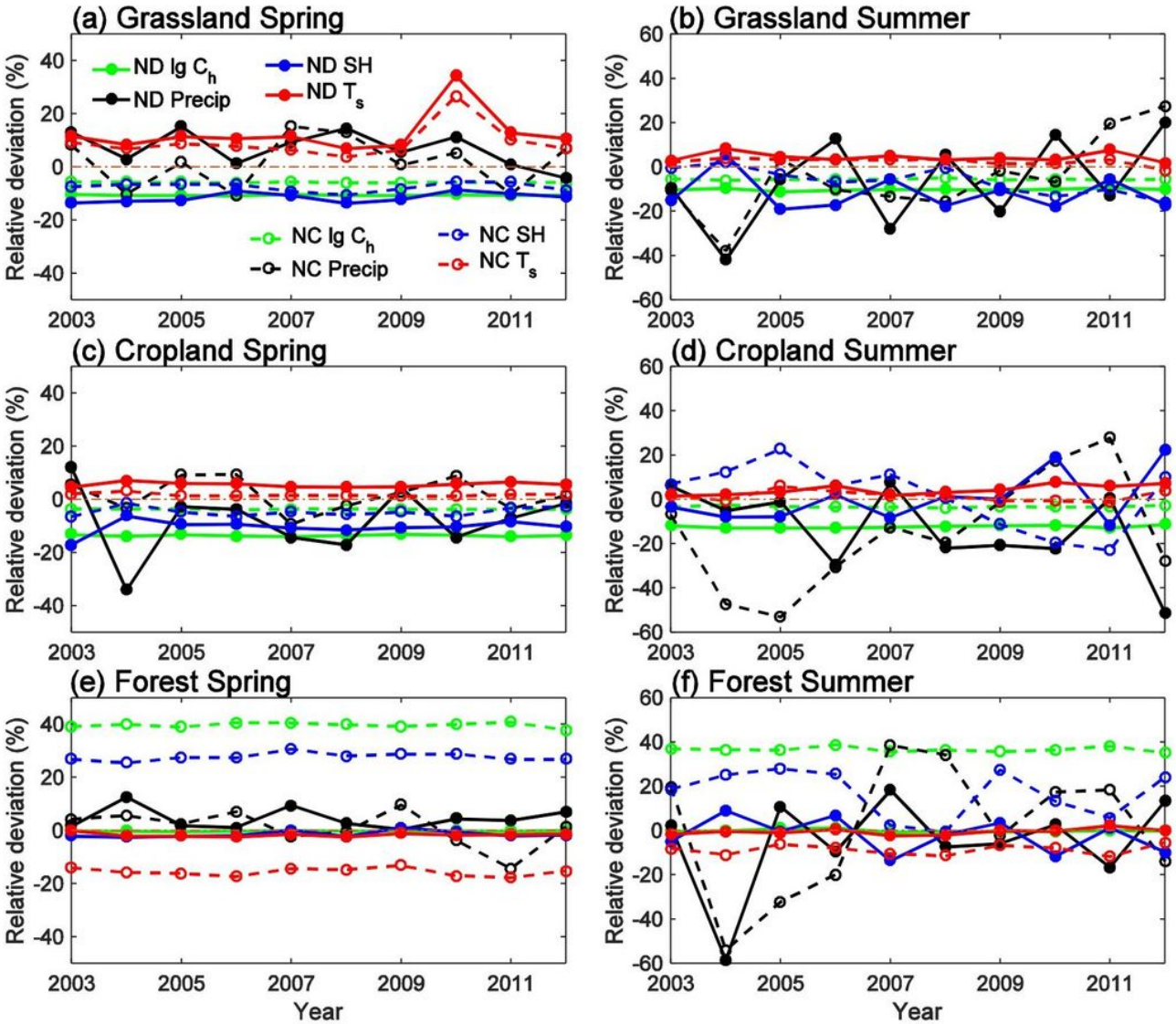

Figure 13

The deviations in Ch (plotted at log10 scale), sensible heat flux (SH), precipitation (Precip), and land surface temperature (Ts) between the simulations using the default M–O (Default), Czil = 0.1 (Czil), and Czil-h (Newczil) schemes at (a– b) grassland, (c–d) cropland, and (e–f) forest during 2003–2012. ND: (Newczil – Default) / |Newczil|×100, NC: (Newczil – Czil) / |Newczil|×100

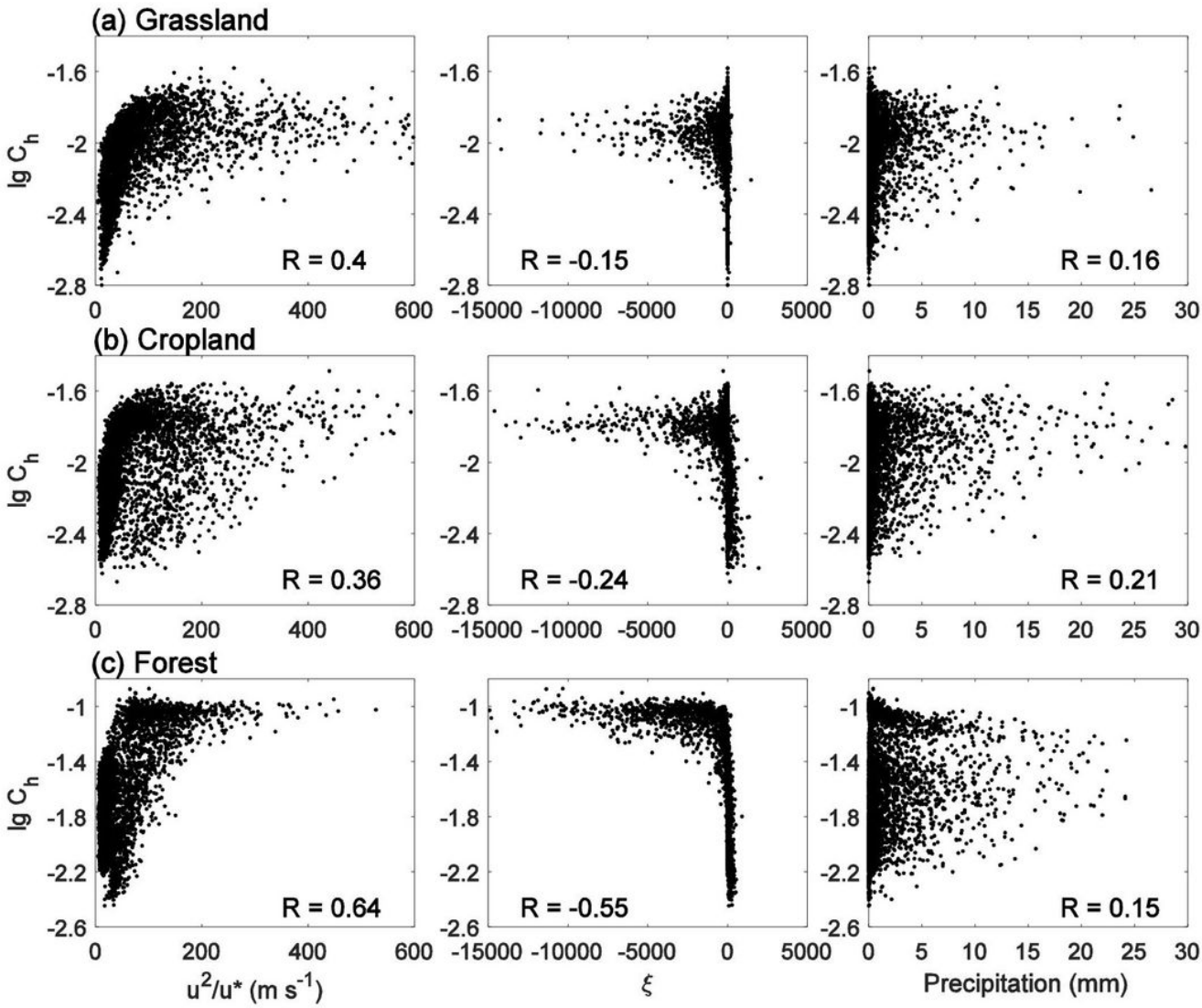

Figure 14

Scatter distributions at (a) grassland, (b) cropland, and (c) forest between the 6-hourly Ch (plotted at log10 scale) and the dynamic comprehensive variable (u2 /u*), the Monin–Obukhov stability parameter (ζ) and precipitation simulated by the Czil-h scheme during 2003–2012 summer. The u2 /u* is the ratio of surface wind speed (u) squared and friction velocity (u*), and the ζ is the ratio of reference height and Monin-Obukhov length (the detailed calculation seen in Eq. 5). Pearson correlation coefficient between the simulations and the observations (R) is displayed in each panel

Supplementary Files

This is a list of supplementary files associated with this preprint. Click to download.

- CHinChinaWRFtable.pdf